Water Resources Research

RESEARCH ARTICLE
10.1029/2023WR035387

Estimation of Capillary-Associated NAPL-Water Interfacial Areas for Unconsolidated Porous Media by Kinetic Interface Sensitive (KIS) Tracer Method

Alexandru Tatomir[1,2], Huhao Gao[1], Hiwa Abdullah[1], Christopher Pötzl[3], Nikolaos Karadimitriou[4], Holger Steeb[4], Tobias Licha[5], Holger Class[6], Rainer Helmig[6], and Martin Sauter[1,7]

[1]Department of Applied Geology, Geoscience Centre of the University of Göttingen, Göttingen, Germany, [2]Independent Researcher, Göttingen, Germany, [3]Department of Structural Geology and Geodynamics, Geoscience Centre of the University of Göttingen, Göttingen, Germany, [4]Department of Structural Engineering, University of Stuttgart, Stuttgart, Germany, [5]Department of Applied Geology, Institute of Geology, Mineralogy and Geophysics, Ruhr University Bochum, Bochum, Germany, [6]Department of Hydromechanics and Modelling of Hydrosystems, University of Stuttgart, Stuttgart, Germany, [7]Leibniz Institute for Applied Geophysics, Hannover, Germany

Key Points:

- The capillary-associated interfacial area is measured with the kinetic interface sensitive tracer method in six unconsolidated porous media
- It is found the maximum specific capillary-associated interfacial area is linearly correlated to the inverse mean grain diameters
- The higher capillary-associated interfacial area is found in natural porous media due to surface roughness and irregular grain shapes

Supporting Information:

Supporting Information may be found in the online version of this article.

Correspondence to:

H. Gao,
huhao.gao@uni-goettingen.de

Citation:

Tatomir, A., Gao, H., Abdullah, H., Pötzl, C., Karadimitriou, N., Steeb, H., et al. (2023). Estimation of capillary-associated NAPL-water interfacial areas for unconsolidated porous media by kinetic interface sensitive (KIS) tracer method. *Water Resources Research*, *59*, e2023WR035387. https://doi.org/10.1029/2023WR035387

Received 3 JUN 2023
Accepted 10 NOV 2023

Author Contributions:

Conceptualization: Alexandru Tatomir, Huhao Gao, Rainer Helmig, Martin Sauter
Data curation: Alexandru Tatomir, Huhao Gao, Hiwa Abdullah, Christopher Pötzl
Formal analysis: Alexandru Tatomir, Huhao Gao, Hiwa Abdullah
Funding acquisition: Alexandru Tatomir, Nikolaos Karadimitriou, Holger Steeb, Martin Sauter

Abstract By employing kinetic interface sensitive (KIS) tracers, we investigate three different types of glass-bead materials and three natural porous media systems to quantitatively characterize the influence of the porous-medium grain-, pore-size and texture on the specific capillary-associated interfacial area (FIFA) between an organic liquid and water. By interpreting the breakthrough curves (BTCs) of the reaction product of the KIS tracer hydrolysis, we obtain a relation for the specific IFA and wetting phase saturation. The immiscible displacement process coupled with the reactive tracer transport across the fluid–fluid interface is simulated with a Darcy-scale numerical model. Linear relations between the specific capillary-associated FIFA and the inverse mean grain diameter can be established for measurements with glass beads and natural soils. We find that the grain size has minimal effect on the capillary-associated FIFA for unconsolidated porous media formed by glass beads. Conversely, for unconsolidated porous media formed by natural soils, the capillary-associated FIFA linearly increases with the inverse mean grain diameter, and it is much larger than that from glass beads. This indicates that the surface roughness and the irregular shape of the grains can cause the capillary-associated FIFA to increase. The results are also compared with the data collected from literature, measured with high resolution microtomography and partitioning tracer methods. Our study considerably expands the applicability range of the KIS tracers and enhances the confidence in the robustness of the method.

1. Introduction

The interfacial area between fluid phases plays a critical role in the coupled multiphase flow, solute transport and reaction processes in porous media (Hassanizadeh & Gray, 1990; Reeves & Celia, 1996). Some applications, where the fluid–fluid interfacial area (FIFA) plays a significant role, are the geological storage of CO_2 (e.g., Niemi et al., 2016), oil and gas recovery, the remediation of contaminated sites, such as from nonaqueous phase liquid (Miller et al., 1990), per- and poly-fluoroalkyl substances (e.g., Brusseau, 2018, 2019), etc.

The fluid–fluid interfacial areas can be classified in capillary-associated FIFA (e.g., terminal menisci and corner interfaces), and film-associated (or surface-adsorbed) interfacial areas (Brusseau et al., 2006; Costanza-Robinson & Brusseau, 2002; Porter et al., 2010; Figure 1a). The sum of the two represents the total interfacial area.

1.1. Models for Calculating the FIFA

Due to difficulties in directly measuring the FIFA, initial studies focused on developing theoretical and modeling approaches employing normalized interfacial area per unit of representative elementary volume (Bradford & Leij, 1997; Cary, 1994; Dalla et al., 2002; Dobson et al., 2006; Gvirtzman & Roberts, 1991; Hassanizadeh & Gray, 1993; Held & Celia, 2001; Leverett, 1941; Oostrom et al., 2001; Reeves & Celia, 1996). The models can be classified into the following categories: pore-geometry models, where the porous medium is represented using an idealized spherical packing (e.g., Gvirtzman & Roberts, 1991; Likos & Jaafar, 2013), or a bundle of capillary tubes (Cary, 1994; Oostrom et al., 2001), and thermodynamic-based models (Bradford & Leij, 1997; Grant & Gerhard, 2007; Leverett, 1941) measuring the net amount of reversible work. With the development of

Investigation: Alexandru Tatomir, Huhao Gao, Hiwa Abdullah, Christopher Pötzl, Nikolaos Karadimitriou, Holger Steeb, Holger Class, Martin Sauter
Methodology: Alexandru Tatomir, Huhao Gao, Hiwa Abdullah, Christopher Pötzl, Nikolaos Karadimitriou, Tobias Licha, Holger Class, Rainer Helmig, Martin Sauter
Project Administration: Alexandru Tatomir, Nikolaos Karadimitriou, Holger Steeb, Martin Sauter
Resources: Alexandru Tatomir, Huhao Gao, Hiwa Abdullah, Christopher Pötzl, Nikolaos Karadimitriou, Tobias Licha, Holger Class, Rainer Helmig, Martin Sauter
Software: Alexandru Tatomir, Huhao Gao
Supervision: Alexandru Tatomir, Nikolaos Karadimitriou, Holger Steeb, Rainer Helmig, Martin Sauter
Validation: Alexandru Tatomir, Huhao Gao, Hiwa Abdullah, Nikolaos Karadimitriou, Tobias Licha
Visualization: Alexandru Tatomir, Huhao Gao
Writing – original draft: Alexandru Tatomir, Huhao Gao
Writing – review & editing: Alexandru Tatomir, Huhao Gao, Nikolaos Karadimitriou, Holger Steeb, Tobias Licha, Holger Class, Rainer Helmig, Martin Sauter

computational capabilities other categories were added: pore-network models that use a simplified representation of the porous medium as a network of pore-bodies and pore-throats (Reeves & Celia, 1996); pore-morphology models (e.g., Dalla et al., 2002); and direct pore-scale numerical simulations using particle-based methods such as the Lattice Boltzmann (Porter et al., 2010), smooth particle hydrodynamics, and grid-based computational fluid dynamics methods, such as the level-set-, volume-of-fluid-, and phase field-methods (Meakin & Tartakovsky, 2009). The pore-scale models calculate explicitly the magnitude of FIFA and allow for the calculation of upscaled per-volume normalized quantities, that is, capillary pressure, saturation and specific interfacial areas, required by the continuum-based, Darcy-scale multiphase flow simulators. The expression of the FIFA as volume averaged quantity allows its straightforward implementation into the Darcy-scale type flow simulators, since no additional parameters other than the initial ones are required.

1.2. Measurement Techniques for Fluid–Fluid Interfacial Area

Several experimental methods were proposed to measure the fluid–fluid interfacial areas (FIFAs): interface partitioning tracer test (IPTT), where the tracer is dissolved in an aqueous (Anwar et al., 2000; Brusseau et al., 2007; Kim et al., 1997; Saripalli et al., 1997) or in a gaseous (Costanza-Robinson & Brusseau, 2002; Kim et al., 1999) phase, high-resolution industrial X-ray microtomography (XMT), and synchrotron XMT (Araujo & Brusseau, 2020; Brusseau et al., 2008; Culligan et al., 2006; McDonald et al., 2016; Narter & Brusseau, 2010; Patmonoaji et al., 2018; Peche et al., 2016; Porter et al., 2010; Ying et al., 2017), the gas adsorption chemical reaction (Ying et al., 2017), experiments using microfluidic devices (Karadimitriou et al., 2016), and the kinetic interface sensitive tracer method (Tatomir et al., 2018). The experimental methods for measuring the FIFA are usually applied in controlled laboratory conditions, that is, tracer methods, XMT, micro models (e.g., Dobson et al., 2006; Karadimitriou et al., 2016; McDonald et al., 2016; Porter et al., 2010; Tatomir et al., 2018), but also in the field, that is, tracer methods (Annable et al., 1998; Nelson & Brusseau, 1996; Simon & Brusseau, 2007). Some methods are inherently designed for laboratory conditions only, for example, micro-models, and XMT.

Usually, standard tracer techniques measure the FIFA under steady state conditions, when a residual saturation is formed. For instance, the gas-phase IPTT implies that a residual water saturation is created in the column, while the gas phase together with two tracers, a conservative and a reactive one, are being circulated. The tracer partitioning on the fluid–fluid interface is interpreted from the breakthrough curves (BTCs) and the FIFA is calculated. Most of the literature related to the measurement of FIFA address to air-water fluid systems. However, there is a consistent body of literature which addresses the NAPL-water or organic fluid-water fluid systems (Brusseau et al., 2008, 2009, 2010; Cho & Annable, 2005; Dobson et al., 2006; Narter & Brusseau, 2010; Schnaar & Brusseau, 2006; Tatomir et al., 2018; Zhong et al., 2016).

The kinetic interface sensitive (KIS) tracer method was proposed by Tatomir et al. (2018) for quantifying the FIFA in a dynamic immiscible displacement process. KIS tracers are a category of non-polar, hydrolyzable phenolic esters (Schaffer et al., 2013). In contact with water, they undergo an irreversible, pseudo zero-order reaction at the fluid–fluid interface to form two highly soluble products, that is, an acid and a phenol, Equation 1. Their non-polarity allows KIS tracers to be dissolved in non-polar liquids, for example, n-octane, while the reaction product Naphthalene-2-Sulfonic Acid (2-NSA) is water soluble, as shown in Figure 1b. Thus, the reaction (interphase mass transfer) is only controlled by the interfacial area. By measuring the reacted acid in the water, we are able to back-calculate the interfacial area. Due to the pronounced fluorescent properties of the product acid, the detection is performed by a fluorescence spectrophotometer.

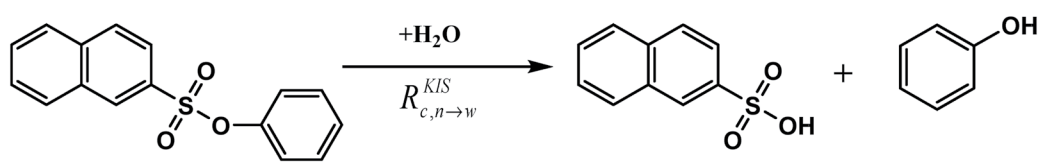

Phenyl Naphthalene-2-Sulfonate
λ = 280 nm → 343 nm

Naphthalene-2-Sulfonic Acid
λ = 225 nm → 338 nm

Phenol
λ = 269 nm → 296 nm

(1)

where $R^{KIS}_{c,n\rightarrow w}$, is the reaction rate constant, determined in static batch experiments.

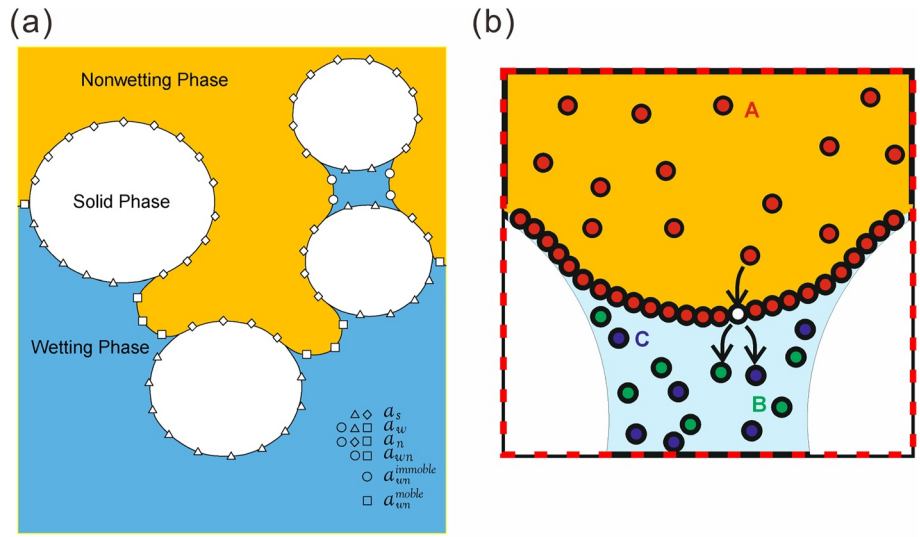

Figure 1. (a) Illustration of the different types of interfacial areas during a dynamic displacement process (a_{wn} capillary-associated FIFA, a_n area of the non-wetting phase; a_w area of the wetting phase; a_s area of the solid phase); (b) KIS tracer (a) adsorption on the fluid–fluid interface, followed by hydrolysis to form two by-products (B + C) dissolved in water, an acid and a phenol, modified from Porter et al. (2010) and Tatomir et al. (2018).

The concept of the KIS tracer method has been proven by controlled column experiments with a well-characterized glass-bead porous medium (Tatomir et al., 2018). The experimental results were interpreted by specifically developed numerical models for multiphase flow coupled with reactive transport, showing a general agreement of the FIFA size with the theory. The interpretation of the BTCs of the product acid provides information about the size of the FIFA.

1.3. Studies Comparing the Experimental Methods for FIFA Measurement

A particular measurement technique can quantify, either the total interfacial area, the capillary-associated FIFA, or some combination of both the capillary-associated FIFA and some part of the film associated area. Compared to aqueous-phase IPTT the gas-phase IPTT generally yields larger FIFA (Costanza-Robinson & Brusseau, 2002). It is hypothesized that the gas-phase IPTT measures both capillary and film-adsorbed FIFA while the aqueous-phase IPTT measures primarily FIFA formed by water held by capillarity, for example, pendular rings. At low water saturations the FIFA measured with gas-phase IPTT showed exponential increase with saturation (Costanza-Robinson & Brusseau, 2002; Kim et al., 1999; Peng & Brusseau, 2005). Similarly, using gas-phase IPTT, Peng and Brusseau (2005) showed that at low water saturations, the maximum air-water FIFA approached those of the normalized solid surface areas. This indicates that indeed the gas phase IPTT measures the total FIFA, as this was orders of magnitude larger than the calculated geometric smooth-sphere specific solid surface area (GSSA), but in good agreement with the specific solid surface area (SSSA) measured with the Nitrogen Brunauer–Emmett–Teller method (N_2/BET).

Several studies reported that IPTT-measured FIFAs were larger than those measured with XMT, which can only scan with a certain spatial resolution (Brusseau et al., 2006, 2007, 2010, 2015; McDonald et al., 2016). Narter and Brusseau (2010) compared the aqueous-phase IPTT with high-resolution micro-tomography for an organic liquid-water-glass bead porous medium system, in an attempt to address the hypothesis that the surface roughness has an influence on the FIFA. Their findings suggest that IPTT can provide FIFA values similar to those obtained from computed micro-tomography when the porous medium has no surface roughness. In that sense, the maximum specific FIFA, was found to be similar to the SSSA measured using N_2/BET and using the smooth-sphere assumption (Narter & Brusseau, 2010; Zhong et al., 2016; Ying et al., 2017). Because with limited resolution, the computed micro-tomography measured FIFAs do not include areas associated with microscopic surface heterogeneities, that is, roughness-associated surface area (Brusseau et al., 2009, 2010). A review of the tracer-based methods for measuring air-water FIFAs is provided in (Costanza-Robinson & Brusseau, 2002), while the various sources of error of the IPTT are discussed in (Brusseau et al., 2008).

Note that relations between the capillary-associated FIFA and the size of the total interfacial area can be established. Grant and Gerhard (2007) used the previous pore-network data of Dalla et al. (2002) to obtain the ratio of capillary-associated FIFA to total FIFA as a function of the saturation. Thus, the total FIFA obtained from their thermodynamic model is able to be related to capillary-associated FIFA for a given fluid saturation.

1.4. Effects of Porous Media Characteristics on FIFA

At the macro-scale, the FIFA is usually expressed as a function of fluid saturation. Literature studies have shown that the grain texture (characteristics) of the porous medium has an effect on the FIFAs. In specific, porous media with larger solid surface areas generate larger fluid–fluid interfacial areas. Several studies demonstrate that fluid–fluid interfacial area is a function of soil properties such as grain size, grain size distribution, and surface roughness (Anwar et al., 2000; Brusseau et al., 2008, 2009, 2010; Cary, 1994; Cho & Annable, 2005; Dobson et al., 2006; Jiang et al., 2020; Peng & Brusseau, 2005). In the following, the available studies of major relevance on the influence of these parameters are described.

1.4.1. Grain-Size Influence on Fluid–Fluid Interfacial Area

Both the FIFA models and experiments show that the maximum total specific FIFA is a function of the inverse median grain diameter (e.g., Anwar et al., 2000; Brusseau et al., 2009). Costanza and Brusseau (2000) used the theoretical model-based data reported by Cary (1994) to evaluate the influence of the porous-medium grain size on the FIFA. One observation of these studies was that porous media with smaller grain sizes have larger specific FIFAs. Using four high purity sands, Dobson et al. (2006) conducted aqueous-phase interface-partitioning tracer tests in NAPL-water fluid systems and compared the results with the theoretical models (Bradford & Leij, 1997; Oostrom et al., 2001) and a modified version of Bradford and Leij (1997). Even though the measured specific FIFA was increasing with decreasing median grain diameter, three out of four reported experimental results were following the theoretically expected trend. Brusseau et al. (2009) use 10 porous media to study the influence of the grain-size and texture on the FIFA. The results show that the specific FIFA and maximum specific FIFA correlate very well with the inverse grain diameter. Also, the FIFA correlates with SSSA and with the inverse median grain diameter (IMGD). This, however, is obtained with tracer techniques which are indirect measurements of the FIFA (Brusseau et al., 2009).

1.4.2. Porous-Medium-Texture Influence on the Fluid–Fluid Interfacial Area

Besides the mean grain diameter, surface roughness is one of the key parameters influencing not only the fluid–fluid interface, but also the degree of wettability, the permeability of the medium, or the capillary pressure- and relative permeability-saturation relations. Peng and Brusseau (2005) used the gas phase IPTT to measure the air-water FIFA for eight soils and natural sands. The values were compared to the normalized surface areas of the porous media. It was observed that FIFAs were generally larger for materials with larger SSSA measured with the N_2/BET method, incorporating the surface roughness. Analyzing 10 different types of porous media, comprising different grain-size distributions and geochemical properties, Brusseau et al. (2009) report that grain-size distributions have minimal impact on the FIFA. Brusseau et al. (2010) conducted aqueous phase IPTTs on two soils (Vinton and Eustis) and found that the maximum NAPL -water FIFAs are much larger than those obtained by geometric calculations with the smooth-sphere assumption, that is, GSSA. Their observations suggest that the surface roughness has a significant impact on the total interfacial area and that the glass beads' total specific FIFA is similar to the SSSA predicted using the smooth-sphere assumption. A linear relation between the total solid area measured with the N_2/BET and the IPTT-measured FIFA is established. However, this is based on seven measurements, with one large N_2/BET value dominant. Because the film-associated areas are a significant component of the FIFAs measured with IPTT, they conclude that the IPTT methods measure some fraction of the interfacial area associated with surface roughness. The findings are further confirmed by Zhong et al. (2016), who used a modified version of aqueous-phase IPTT to measure FIFA at higher saturations than residual, for several porous media made of glass beads, sand and Vinton soil during a series of drainage and imbibition tests. Recently, Jiang et al. (2020) investigated the role of microscale surface roughness on the FIFA assuming a triangular bundle-of-cylindrical capillaries, and their model belonging to the pore-geometry model category. The exponential increase of the total FIFA observed with the gas-phase IPTT method when wetting saturation approaches zero can be explained by the impact of surface roughness on the film-associated FIFA.

Table 1
Summary of Characteristic Properties of the Porous Media Used in the KIS Tracer Two-Phase Flow Experiments

Parameter name	Unit	Symbol	GB55	GB170	GB240	NS130	NS210	NS250
Porosity	(−)	ϕ	0.41	0.42	0.42	0.42	0.42	0.4
d_{50} mean grain diameter	(μm)	d_{50}	55	167	240	132	206	248
d_{10}	(μm)	d_{10}	20	140	205	98	161	198
d_{60}	(μm)	d_{60}	57	172	244	138	214	258
Uniformity coefficient $C_u = d_{60}/d_{10}$	(−)	C_u	2.85	1.23	1.19	1.41	1.33	1.30
Mean pore diameter[a] (see Figure S1 in Supporting Information S1)	(μm)	p_{50}	23.28	73.15	101.35	30.15	61.69	75.01
Pore uniformity coefficient[a] $P_u = p_{60}/p_{10}$	(−)	P_u	1.67	1.51	1.67	1.68	1.75	2.34
SSSA- MIP (Rootare & Prenzlow, 1967)	(cm^{-1})		648	558	129	7122	434	285
GSSA = $6(1-\phi)/d_{50}$	(cm^{-1})		643	196	134		165	134
Bulk density	(g/cm^3)	ρ_b	1.65	1.65	1.6	1.47	1.65	1.67
Lambda (Brooks-Corey)	(−)	λ	3.614	3.606	3.650	3.25	2.925	2.663
Contact angle n-octane -water	(°)	θ	32 ± 6	34 ± 9	10 ± 3	32 ± 10	32 ± 10	32 ± 10
Entry pressure	(Pa)	p_d	5937	1819	1606	4336	2050	1642
Residual wetting phase saturation	(−)	S_{wr}	0.024	0.00	0.016	0.024	0.015	0.051
Longitudinal dispersivity	(m)	α_L	1e−3	1e−3	1e−3	1e−3	1e−3	1e−3
Transversal dispersivity	(m)	α_T	1e−5	1e−5	1e−5	1e−5	1e−5	1e−5
Feret diameter(mm)	(mm)		0.054	0.173	0.24	0.135	0.245	0.273
Circularity	(−)		0.857	0.855	0.898	0.613	0.676	0.593
Aspect ratio	(−)		1.062	1.065	1.018	1.574	1.457	1.59
Roundness	(−)		0.95	0.955	0.983	0.672	0.713	0.701

[a]Based on mercury intrusion porosimetry measurements.

1.5. Objective

To date, the KIS tracer method has been tested only for an ideal porous medium formed by well-sorted glass beads. An important step in developing the KIS tracer method is implementing the method in the laboratory column experiments for different soil types followed by interpreting and comparing the results. Two categories of porous media are to be used, that is, glass-beads and natural sands with different textures, grain- and pore-size distributions. Our objective is to prove the ability of the KIS tracer method to measure the capillary-associated FIFA in porous media formed by various types of sands, and to understand the influence of grain size and surface roughness on the capillary-associated FIFA during primary drainage.

The article is structured as follows: Section 2 explains the details of the methodology, including the study of the porous media materials, the KIS tracer reaction kinetics, the column experiment setups, and the numerical model for interpretation of the results; Section 3 demonstrates the results for the breakthrough curves, the comparison between the experimental data and modeling results, and the comparison between the capillary-associated FIFA measured by the KIS tracer and the published experimental data using various measurement techniques and models; and finally Section 4 lists the main conclusions.

2. Methods

2.1. Materials

2.1.1. Porous Media Grains

Six porous media, three glass-bead media, and three natural sands are used to investigate the influence of the grain size and texture on n-octane-water interfacial area. The quartz sands were commercially purchased. The characteristic properties of the porous media are described in Table 1. Examples of microscopic images of the grains and the grain-size distributions obtained by digital image analysis performed on these images are shown

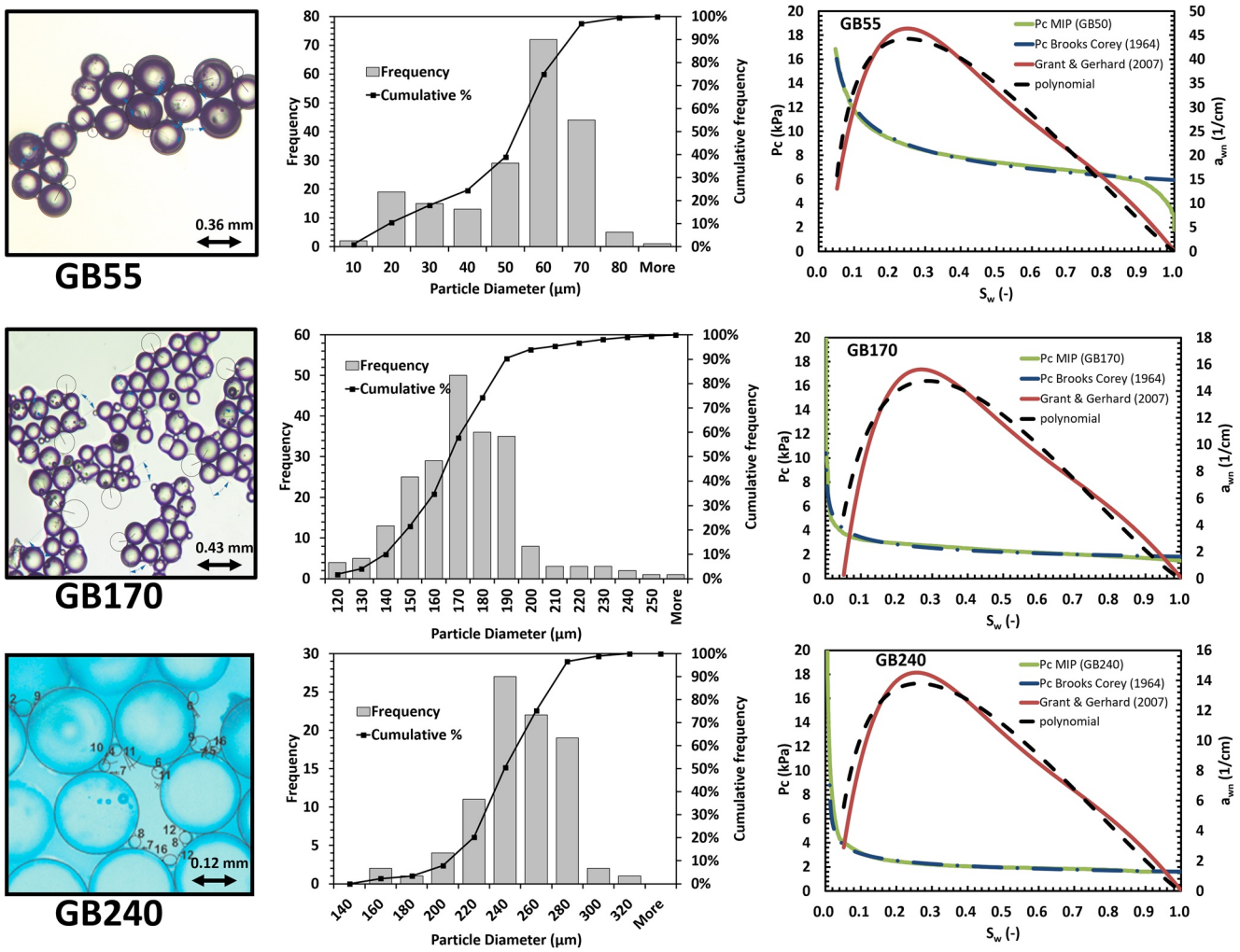

Figure 2. Characterization of the porous media used in the KIS tracer experiments: three glass beads (GB55, GB170, and GB240). Digital illustration of a few grains on a glass sheet (left column), grain-size distribution with the cumulative frequency curve (middle), capillary pressure-saturation, $p_c - S_w$ relation determined with MIP, and the calculated $a_{wn} - S_w$ relation with the explicit interfacial area model of Grant and Gerhard (2007) (right column).

in Figures 2 and 3. The images were processed using ImageJ™ software to determine the grain-diameters, roundness, Feret diameter, aspect ratio (between the major axis and the minor axis when the grain is fitted to an ellipse) and circularity (Tatomir, Halisch, et al., 2016). The three glass-bead porous media are a very fine sand (10–80 μm, d_{50} = 55 μm), a fine sand GB170 (120–230 μm, d_{50} = 170 μm), and fine-to-medium sand GB240 (160–320 μm, d_{50} = 240 μm). GB240 from the company GRACE™ (Glass beads 80/60 mesh) is well sorted with a shallow spectrum of the sand size distributions. The natural-sand porous media can be described as fine sand NS130 (80–200 μm, d_{50} = 130 μm), fine-to-medium sand NS210 (120–320 μm, d_{50} = 210 μm), and medium sand NS250 (180–380 μm, d_{50} = 250 μm).

The capillary pressuresaturation relations were determined by mercury-intrusion porosimetry (MIP). To scale the relations to the n-octane-water system, we used the contact angles, $\theta_{o,w}$, which were determined using digital image analysis on microscopic images. The images are obtained under microscope for the sands mixed with n-octane and water on the glass sheet (Table 1). The conversion of an air-mercury system to an octane-water system is accomplished by rearranging the terms in the Washburn relation as given in Equation 2.

$$p_{c_{o,w}} = p_{c_{Hg,a}} \frac{\sigma_{o,w} \cos\theta_{o,w}}{\sigma_{Hg,a} \cos\theta_{Hg,a}} \tag{2}$$

where $p_{c_{w,o}}$ and $p_{c_{Hg,a}}$ are the capillary pressure for the water-octane fluid system and mercury-air respectively. The mercuryair contact angle $\theta_{Hg,a}$ is 140° and $\sigma_{Hg,a}$ is 480 mN•m^{-1}. $\sigma_{o,w}$, the interfacial tension of

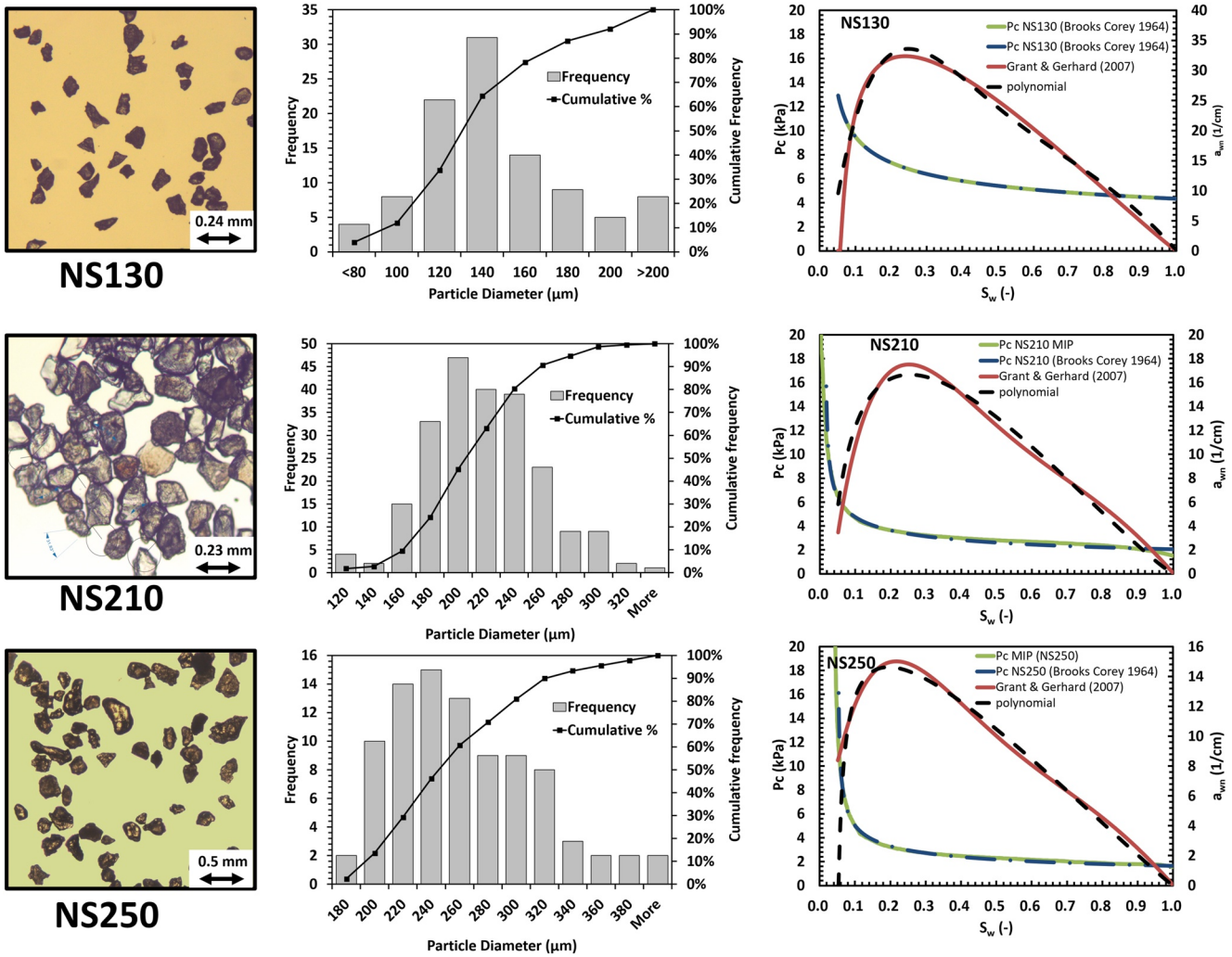

Figure 3. Characterization of the porous media used in the KIS tracer experiments: three natural sands (NS130, NS210, and NS250). Digital illustration of a few grains on a glass sheet (left column), grain-size distribution with the cumulative frequency curve (middle), capillary pressure-saturation, $p_c - S_w$ relation determined with MIP, and the calculated $a_{wn} - S_w$ relation with the explicit interfacial area model of Grant and Gerhard (2007) (right column).

water-n-octane is 50.8 mN•m^{-1} at room temperature (Fukunishi et al., 1996). The capillary pressuresaturation relation curves from MIP were fitted to those of the Brooks and Corey (1964) model by minimizing the root mean square error when determining the pore-size index λ, entry pressure p_e, and residual water saturation, S_{wr} in Equation 3:

$$p_c(S_w) = p_d \left(\frac{S_w - S_{wr}}{1 - S_{wr}} \right)^{-1/\lambda} \tag{3}$$

A high value of the pore index λ corresponds to a flat curve from the entry pressure, $S_w = 1$, until reaching the residual saturation values, indicating the medium is well-sorted and implicitly the pore-throats are of equivalent size.

The glass beads are spherical and of uniform diameter, and therefore, the theoretical specific solid surface area can be calculated using the smooth-sphere assumption expressed in cm^{-1} using Equation 4 or in m^2/g, using Equation 5 (Costanza-Robinson & Brusseau, 2002; Peng & Brusseau, 2005):

$$\mathrm{GSSA}\left(\mathrm{cm}^{-1}\right) = \frac{6(1-\phi)}{d_{50}} \tag{4}$$

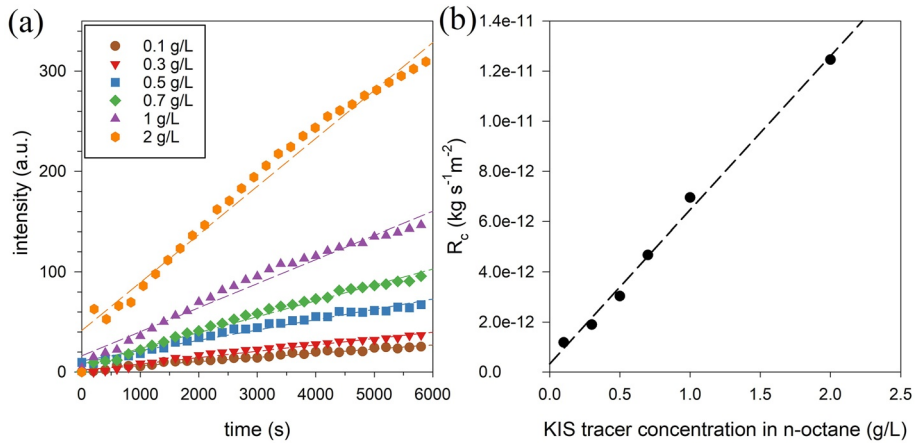

Figure 4. Measured kinetic rates in static batch experiments. (a) 2-NSA concentration reaction rates over time expressed in intensity units as a function of initial 2-NSAPh concentration in n-octane (the regression lines at each concentration are plotted in dashed lines). (b) Calculated hydrolysis reaction rates as a function of initial 2-NSAPh concentration using the experiments in subfigure (a) (the regression lines is plotted in dashed lines). Here, the unit of intensity (a) $u = 86.293 \cdot c_{2\mathrm{NSA}} + 62.6$.

$$\mathrm{GSSA}\left(\mathrm{m}^2/\mathrm{g}\right) = \frac{6}{d_{50}\rho_p} \tag{5}$$

where d_{50} is the mean particle diameter (cm) and ρ_p is the particle density which is 2.65 g cm^{-3}.

The theoretical total interfacial areas can be estimated based on geometrical calculations for smooth spheres and compared to the specific solid surface areas measured with the MIP method, SSSA-MIP.

2.1.2. The KIS Tracer Reaction Kinetics

The pseudo zero-order hydrolysis reaction of the KIS tracer at the fluid–fluid interface has been proven with static batch experiments, showing a linear increase of the concentration up to 2,000–3,000 min (Schaffer et al., 2013). Tatomir et al. (2018) found that the reaction rate is dependent on the initial concentration of the KIS tracer in the non-wetting phase. Generally, a higher reaction rate is preferable to obtain higher 2NSA concentrations in water, because they can be better detected and measured with the fluorescence spectrophotometer. Using an initial concentration up to 2 g/l KIS tracer, we extend our previous range of testing which was up to 0.7 g/l (Tatomir et al., 2018). The setup of the static batch experiments is the same as that in Schaffer et al. (2013). A brief explanation of the setup can be found in Figure S2 of Supporting Information S1. The 2-NSA intensity measured with respect to time for tracer concentration ranging between 0.1 and 2 g/L is plotted in Figure 4a. A linear regression across each data points is implemented to determine a single valued kinetic rate at each tracer concentration (the regression lines are given in dashed lines), and the obtained kinetic rate coefficients are plotted in Figure 4b. It can be observed that the resulting kinetic rate coefficient increases linearly with the tracer concentration. At a tracer concentration of 2 g/L, we obtain $R_{n\to w}^{2NSA} = 1.25 \times 10^{-11}$ kg·m^{-2} s. Considering a pseudo zero-order reaction, with a given tracer concentration, the reaction rate is only dependent on the interfacial area. The difference between the static and dynamic conditions (e.g., with local velocity gradients, micro mixing or diffusion processes) has minimal effects on the determined kinetic rates. It worth noting that as the tracer concentration is in the range of g/L and the 2-NSA (reaction product) is in the range of µg/L (with the experimental time scale), the depletion of KIS tracer in the experiment is neglectable. Thus, the kinetic rate can be assumed as constant during the experiments.

The hydrolysis reaction is expressed as:

$$-\frac{dc_\alpha^\kappa}{dt} = r_{n\to w}^\kappa = R_{c\,n\to w}^\kappa a_{wn}, \tag{6}$$

where c_α^κ is the concentration of component κ in phase α, $R_{c\,n\to w}^\kappa$ is the reaction rate constant. For component 2-NSA in water phase, $R_{c\,n\to w}^{2\mathrm{NSA}}$ was determined in static batch experiments. The a_{wn} is the capillary-associated

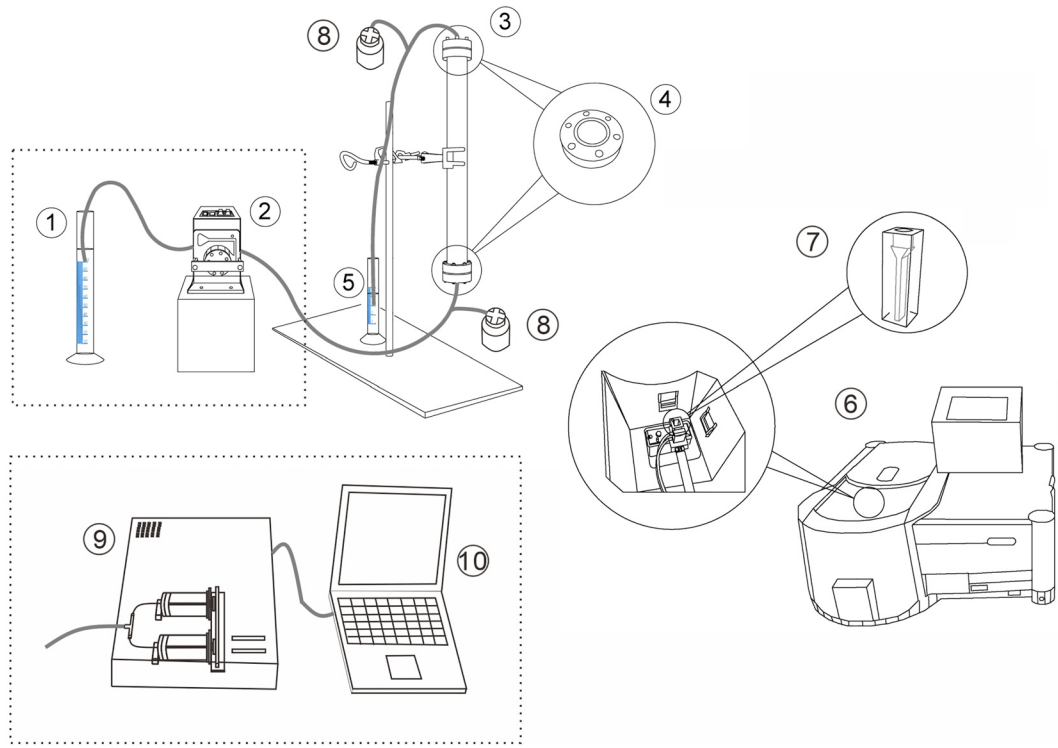

Figure 5. Experimental setup of two-phase flow system. (1) Graded cylinder containing n-octane with dissolved KIS tracer. (2) Peristaltic pump. (3) Sand column. (4) Cap embedded with frit. (5) 5 ml measuring cylinder. (6) Fluorescence spectrophotometer. (7) High precision fluorescence cuvette; (8) External pressure sensors; (9) High-precision syringe pump with two glass syringes; (10) Laptop with a graphical user interface for controlling the pump and recording the data.

FIFA. Following Tatomir et al. (2018), we estimate the a_{wn} using the thermodynamic based, implicit interfacial model proposed by Grant and Gerhard (2007). The model assumes that the interfacial area is dependent on the work done on the system during the displacement, and thus the interfacial area is directly proportional to the area under the pressure-saturation curve. The pressure-saturation curve obtained from the MIP and the interfacial area-saturation relation obtained using the implicit interfacial model are shown in Figures 2 and 3. The details of the implicit interfacial model can be found in Tatomir et al. (2018), and a brief review of the main equations is provided in Text S1 of Supporting Information S1. Then, to put the interfacial area-saturation relation of each sand to a uniform form we performing fitting to the polynomial expression given by Joekar-Niasar and Hassanizadeh (2012). Through the dynamic pore network modeling for multiple drainage and imbibition processes, Joekar-Niasar and Hassanizadeh (2012) found that a functional relation between the FIFA, saturation, and capillary pressure can be expressed using the polynomial expression in Equation 7:

$$a_{wn}(S_w, p_c) = a_0(S_w)^{a_1}(1 - S_w)^{a_2}(p_c^{\max} - p_c)^{a_3} \tag{7}$$

where a_{wn} is the capillary-associated FIFA, S_w is the wetting saturation, p_c is the capillary pressure, a_0,a_1,a_2,a_3, $p_c^{\max}$ are empirically fitted parameters. As the capillary pressure is a function of saturation according to Brooks and Corey's theory (Equation 3), the FIFA here reduces to be only a function of saturation. It is worth noting that this closed form function may not necessary hold true when the flowrate dependency of the interstitial flow structure, the associated size distributions of fluidic elements of the disconnected non-wetting phase, and their effects on the FIFA are taking into consideration (Armstrong et al., 2016; Aursjo et al., 2014; Valavanides et al., 2020).

2.2. Column Experiments Setup

The KIS tracer experimental procedure was developed and described in Tatomir et al. (2018). The technique consists of transient drainage experiments of an initially fully water-saturated column. The drainage/invading fluid is n-octane with KIS tracer dissolved in it. The laboratory experimental results are volumetric outflow BTCs and KIS tracer reaction product in the water phase, that is, 2-NSA concentration BTCs. The experimental apparatus (Figure 5) consists

of a stainless-steel column, 300 mm long and 30 mm in diameter. Two metal frits with extremely fine meshes are placed at either end of the column holding the sand inside the column. A peristaltic pump with adjustable flow rate is first used for saturating the column with water, and later for providing a constant flow to the bottom of the vertically oriented column of n-octane with dissolved KIS tracer. The peristaltic pump can set the rotation speed, but the actual flow rate depends on the permeability of the system. To improve the reproducibility of the experiments and remove small fluctuations in the flow rate, we conducted a second set of experiments using a high-precision syringe pump, neMESYS© Mid Pressure module 1000N from CETONI. It is worth noting that the two pumps impose different boundary conditions on the flow system. The syringe pump directly imposes the volumetric flux of the non-waiting phase at a preselected constant value, while the pressure build-up at the inlet results from the system's response. In contrast, the peristaltic pump imposes cyclic smooth pressure pulses on the feed stream and the injection flux depends on the reaction of the entire flow system. Furthermore, the chemical stability of the materials (e.g., tubings, column) was tested in the presence of ultra-pure water and n-octane. We observed that many carbon-based materials (i.e., tubings) interact with the n-octane inducing either swelling or brittleness. Therefore, only materials which did not react with n-octane were selected when constructing the experimental setup Figure 5. Naphthalenesulfonates are highly fluorescent and can be detected at low concentration levels in the range of µg/L using fluorescence spectrometry. The 2-NSA concentration in water was measured using a Cary Eclipse™ fluorescence spectrophotometer from Varian Inc. The excitation wavelength is 225 nm and the emission wavelength 338 nm.

Before the experiment, the steel-column was packed with dry granular material (i.e., sand, or glass beads). The pouring of sand into the column is along with slight vibrations or more uniform bulk properties. After packing, the column is slowly filled with water from the bottom to avoid air entrapment. The columns are saturated for more than 24 hr by pumping deaired, ultra-pure, deionized water. The porous medium properties are reported in Table 1. The KIS tracer (phenyl naphthalene-2-sulphonate) is dissolved in the non-aqueous phase liquid (n-octane) with concentrations of 0.5 g/l and 2 g/l. The experiments are conducted in two batches with different KIS tracer concentrations: 0.5 g/l for the first batch (EXP_1, 2, 3 with peristaltic pump for GB55, EXP1_pp and EXP2_pp for GB170, EXP_1, 2, 3 with peristaltic pump for NS210); and 2 g/l for the second batch (GB240 experiments).

When the experiment starts, the n-octane (with the KIS tracer dissolved) is injected into the column at a rate between 0.4 and 0.8 ml/min. At the outlet, the two-phase flow BTC was captured by collecting the fluid volumes in a 5 ml graded measuring cylinder. Using a glass pipette, the water containing the reaction product 2-NSA is taken and placed in a 0.5 ml cuvette to be analyzed in the spectrophotometer. A predefined calibration curve allows for the conversion of intensity readings into 2-NSA concentration. Initially, only pure water is drained from the system at the outlet, and the water samples are collected and measured at 5 ml intervals. Just before the arrival of the first n-octane at the outlet, the water sampling intervals are increased to 1 ml to provide the BTCs at a higher temporal resolution. In the experiments, the viscosity ratio between the invading fluid and receding fluid is 0.5, and the capillary numbers (calculated in Table S1 of Supporting Information S1) are between 1.15×10^{-7} and 2.36×10^{-7}. Thus, the experiments are in the range of the capillary fingering regime according to Lenormand et al. (1988). Since the capillary numbers of the experiments are close, potential effects on the flow system induced by the difference in the flowrate intensity are minimal. Thus, the measurement results are mainly to be studied with respect to the differences in sand sizes and textures.

After every experiment, the glass beads and the natural sands are washed and dried for more than 48 hr. The porous steel frits of the columns are washed and dried before each experiment and the packing process is repeated. However, each packing will lead to a different grain geometric configuration, which may lead to differences in petrophysical parameters, that is, permeability and tortuosity, with little influence on porosity. The experiments are done for each of the sand with the setup with the peristaltic pump (pp) or the syringe pump (sp). For GB170, GB240, NS210, experiments are performed with both pump setups. Each experiment is conducted in triplicate to verify the reproducibility of the results.

2.3. Mathematical Modeling and Interpretation of the Results

The interpretation of the experimental results is done using an immiscible two-phase flow model with reactive transport, and it accounts for the specific FIFA (Tatomir et al., 2018). The mathematical model is implemented in COMSOL Multiphysics™. Several models capable of addressing the KIS tracers in multiphase flow in porous-media systems were developed in the past (Tatomir et al., 2013, 2015, 2018; Tatomir, Halisch, et al., 2016; Tatomir, Jyoti, & Sauter, 2016). Besides the immiscible two-phase flow models, a compositional

model investigating the KIS tracer application in supercritical CO_2 brine fluid systems was developed in the DuMu^x simulator (Flemisch et al., 2011; Tatomir et al., 2015). Comparing the two models applied with experimental data, Tatomir et al. (2018) showed only minor differences. Thus, in this study, the results are interpreted by implementing only the COMSOL model.

The details of the mathematical model can be found in Tatomir et al. (2018). Here, we briefly review the main equation to be implemented in the model. The drainage process, defined as the non-wetting phase displacement of the wetting phase, can be mathematically represented by the governing macro-scale equations for immiscible two-phase porous media flow:

$$\frac{\partial(S_\alpha \phi \rho_\alpha)}{\partial t} - \nabla \cdot (\rho_\alpha v_\alpha) - \rho_\alpha q_\alpha = 0, \text{ with } \alpha = w, n \tag{8}$$

$$v_\alpha = -\mathrm{K}\frac{k_{r\alpha}}{\mu_\alpha}(\nabla p_\alpha - \rho_\alpha \mathbf{g}). \tag{9}$$

The system of partial differential Equation 5 is closed with the following equations:

$$S_w + S_n = 1, \tag{10}$$

$$p_n - p_w = p_c, \tag{11}$$

where α denotes the phase (with w, as the wetting phase and n as the non-wetting phase), S_α is the phase saturation, ρ_α is the phase density, ϕ is the porosity of the matrix q_α is the phase source or sink term, K is the intrinsic permeability, $k_{r\alpha}$ is the relative permeability, μ_α is the phase dynamic viscosity, $\mathbf{g}$ is gravitational acceleration, p_α is the phase pressure, p_c denotes the capillary pressure, and v_α is the apparent velocity of the fluid as given by the extended multiphase Darcy's law. The capillary pressure and saturation are according to Equation 2. The relative permeability-saturation relation is written according to the Burdine theorem (Burdine, 1953; Helmig, 1997):

$$k_{rw}(S_w) = S_e^{\frac{2+3\lambda}{\lambda}}, \tag{12}$$

$$k_{rn}(S_w) = (1 - S_e)^2\left(1 - S_e^{\frac{2+\lambda}{\lambda}}\right) \tag{13}$$

where S_{wr} denotes the residual saturation, p_d refers to the entry pressure, λ is the pore-size distribution parameter, and S_e is effective saturation $S_e = (S_w - S_{wr})/(1 - S_{wr})$. The transport of the tracer reacted product (2-NSA) is described by an advection-dispersion-reactive transport equation, which is solved decoupled from the two-phase flow equations, assuming there is no back-partitioning, secondary reactions, or any other mass transfer processes (e.g., n-octane dissolved in water phase, or water in n-octane phase).

$$\frac{\partial(\phi S_w c_w^\kappa)}{\partial t} - \nabla \cdot \left(c_w^\kappa \boldsymbol{v_w} - D_{pm,w}^\kappa \nabla c_w^\kappa\right) + r_{nw\to w}^\kappa = 0, \ \alpha = w, \ n \tag{14}$$

Here, c_w^κ is the concentration of 2-NSA (κ) in the aqueous phase, $D_{pm,w}^\kappa$ is the hydrodynamic dispersion coefficient, and $r_{nw\to w}^\kappa$ denotes the tracer reaction rate over the fluid–fluid interface. The hydrodynamic dispersion coefficient can be calculated as $D_{pm,w}^\kappa = v_w a_L$. The hydrolysis reaction is formulated according to Equation 6, and the interfacial area is modeled by fitting Equation 7 to the thermodynamic model by Grant and Gerhard (2007), refer to Tatomir et al. (2018). The solute dispersivities were determined using fluorescent tracer experiments to be $D_{pm,w}^\kappa = 10^{-3}$ m (Tatomir et al., 2018). Note that dispersivities measured in single-phase flow conditions is not necessarily valid when another fluid-phase is present (Karadimitriou et al., 2016). By applying the root mean square error (RMSE) as a criterion the best fitting curves were found.

A two-step approach is employed to interpret the results. The first step is the calibration of the two-phase flow model to the experiment by performing a sensitivity analysis with respect to flow rate, Q, and intrinsic permeability, K. It is estimated that both have the highest measurement uncertainty, due to the expected small oscillations in the pumping rate (±0.05 ml/min), the unknown influence of repacking the columns, and of the column frits. The peristaltic pump is set to operate at a fixed number of rotations per minute. As pressure in the column and the n-octane reservoir at the inlet changes during the experiment, flow rate fluctuations should be expected. The

Table 2
Fluid and Soil-Fluid Properties

Parameter name	Unit	Symbol	Value/range
Diffusion coefficient	(m^2/s)	D_m	1e−9
Density water	(kg/m^3)	ρ_w	1,000
Density n-octane	(kg/m^3)	ρ_n	703
Viscosity of water	(Pa·s)	μ_w	1.00e−03
Viscosity of n-octane	(Pa·s)	μ_n	5.42e−04
Surface tension n-octane -water [a]	(N/m)	$\sigma_{o,w}$	0.0508
Longitudinal dispersivity [b]	(m)	α_L	1e−3
Transversal dispersivity	(m)	α_T	1e−5

[a]Measurements of surface tension determined by capillary rise method showed no differences between pure n-octane and n-octane with 2 g/l dissolved KIS tracer. [b]Measured by single-phase tracer experiments in the column.

permeabilities of the sand are determined with a falling head permeameter, which may provide a wide range of permeability values. The permeability of the system is affected by the condition of the porous frits and the repacking before each experiment. The modeling parameters determined from the petrophysical characterization of the natural sands and glass beads samples are reported in Table 1 and of the fluid system in Table 2.

Once the outflow volume ratio curves are matched, we proceed with the calibration of the concentration BTCs of the KIS tracer reaction product, that is, 2-NSA. In this sense, a sensitivity analysis using the specific interfacial-area relation, $a_{wn} - S_w$, that is, Equation 7 and its associated parameters as the unknown parameter is conducted. The reaction rate expressed in Equation 6 depends on the reaction rate coefficient, known from experiments and on a_{wn}. Initially, the Grant and Gerhard's model is used to approximate the specific FIFA a_{wn} curves from the MIP measured $p_c - S_w$ relations. Afterward, the polynomial expression in Equation 7 is used to fit the modeled a_{wn}, by finding best fitting parameters, a_0, a_1, a_2, p_c^{max}. This provides the theoretical $a_{wn} - S_w$ of the fluid–fluid porous medium system. The second step comprises the calibration of the KIS reaction product BTCs. This is performed running a parameter sweep on parameter a_0 in Equation 7, while the other parameters a_1, a_2, p_c^{max} remain unchanged. The parameter a_0 controls the maximum specific FIFA, $a_{wn}^{\max}$ while maintaining the general shape of the $S_w - a_{wn}$ curve (Tatomir et al., 2018).

3. Results and Discussion

The experimental and modeling results and the discussions for the six porous media (three glass beads, GB55, GB170, GB240, and three natural sands, NS130, NS210, NS250), are presented in this section.

3.1. Two-Phase Flow Calibration

The calibration of the two-phase flow is done based on the effluent volume of the fluids, while the kinematic variables, for example, pressures, relative permeabilities etc., are estimated from the calibrated model. The kinematic variables are dependent on several factors, for example, the geometry of the repacked unconsolidated media, the condition of the frits, the configuration of the non-wetting phase invading pathways, etc. With the difficulties to identify these factors during each experiment and to simplify the problem, the two-phase flow model here focuses on matching the experimental effluent volumes and breakthrough times which are important for the tracer experiment. The experimental BTCs of the volume fraction of the non-wetting phase to the total fluid volume, together with the simulated BTCs are illustrated in Figure 6. Triplicate experiments are conducted for each glass-beads and quartz sand medium using either the peristaltic pump (pp) or the syringe pump (sp), with the results labeled as EXP1, EXP2, and EXP3. The results using the peristaltic pump show some differences in the breakthrough time due to the higher variations in the flow rates than in the case of the syringe pump. Despite using the same packing procedure (vibrating and adding small increments) and washing and drying the frits before each experiment, slight differences in the porosity and the overall permeability of the formed porous media are inevitable. This makes the reproducibility of the experiments challenging. In contrast, the use of the syringe pump with fixed flow rates resulted in consistent breakthrough times for the triplicate experiments, for each sand type. Table 3 provides the flowrate, permeability, and porosity data of each experiment.

It can be observed that the simulated results from the two-phase flow model can generally match well the experimental BTCs, as shown in Figure 6. However, the volume fraction of the non-wetting phase to total fluid volume (in the outflow) is slightly overestimated by the model for several experiments such as EXP1_pp and EXP3_pp for GB55, and EXP2_pp for GB170. Conversely, the model slightly underestimates the volume fraction of the non-wetting phase to total fluid volume for several experiments where the breakthrough occurred relatively earlier (around 3000s). These experiments include EXP1_sp, EXP2_sp, EXP3_sp with syringe pump for GB170, EXP2_sp and EXP3_sp for GB240, EXP1_sp, EXP2_sp, EXP3_sp with syringe pump for NS210. These deviations are likely due to variations in the $p_c - S_w$ relation used in the model, and to the conversion of the relation from Mercury-Air system (measured by MIP) to Water-Octane system.

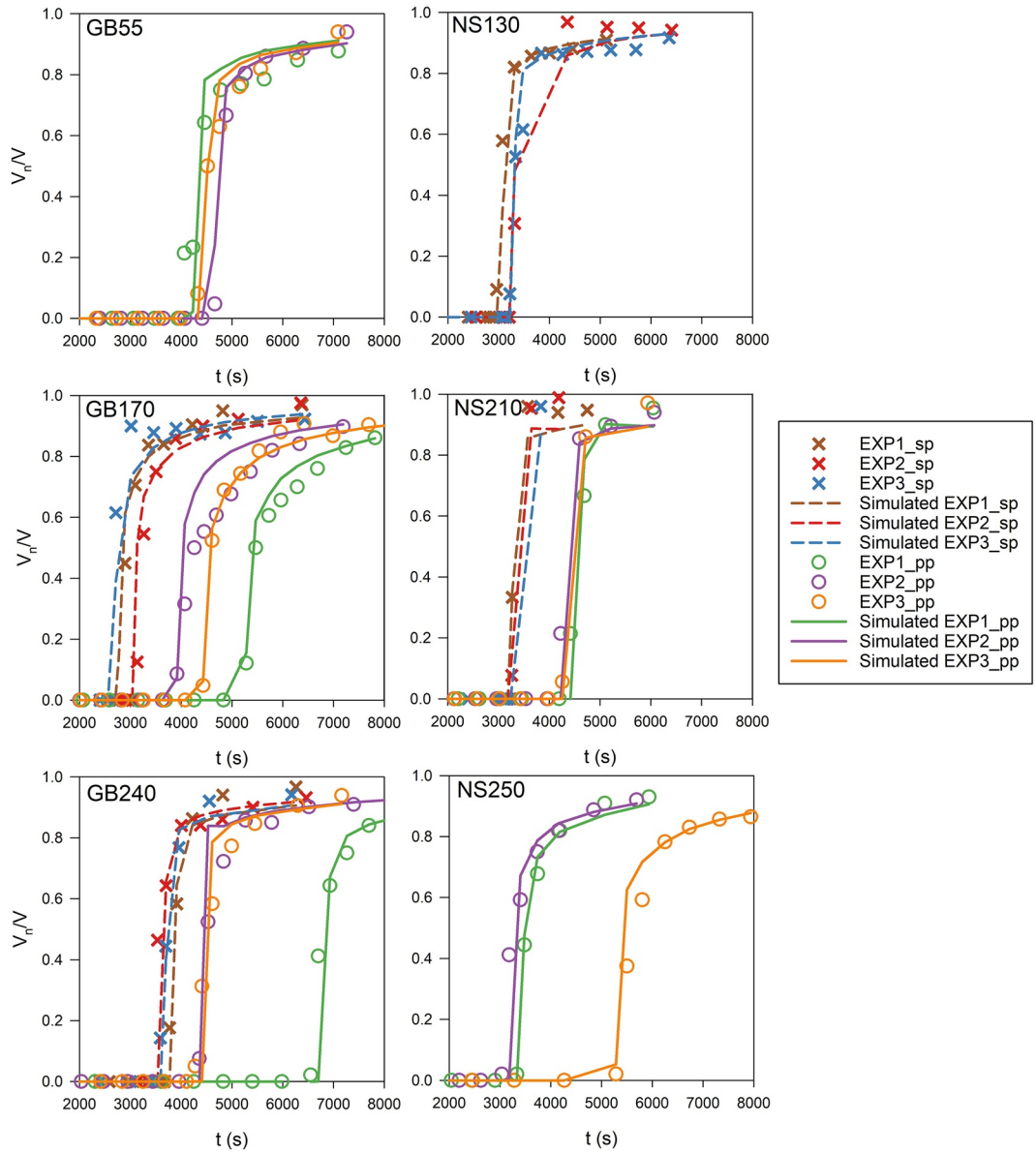

Figure 6. Plot of the breakthrough of the volumetric fraction of the non-wetting phase to the total fluid volume at the column outlet versus time, for experimental data (crosses) and simulated BTCs (dashed lines) of triplicate experiments (EXP1, EXP2, and EXP3) with the peristaltic pump (pp) and the syringe pump (sp).

Furthermore, the BTCs of the volume fraction of the non-wetting phase to total fluid volume from the experiments with the natural sands show a faster change from 0 to 1 compared to those from the experiments with the glass beads. This leads to a smaller volume of displaced water from the column and fewer measurement points, especially for NS130 and NS210. The irregular pore geometries of the unconsolidated porous media induced by the irregular grain geometries of the natural sand grains (with low roundness as shown in Table 1) may explain this phenomenon. The irregular pore geometries likely facilitate the formation of stable flow pathways for fluid displacement, that is, larger pores are preferred by the invading phase, and the possibility of remobilization of the receding phase is reduced. Thus, the volume of water samples obtained after breakthrough is smaller for experiments conducted with natural sands.

3.2. Interpretation of the Hydrolyzed KIS Tracer Reaction Product Breakthrough Curves

The BTCs of the reacted 2-NSA concentration are plotted in Figure 7, with measured 2-NSA concentrations in water ranging between 0 and 12 µg/L. As discussed in Section 2.3, to obtain the specific interfacial area

Table 3
Parameters Applied in the Model to Fit the Experimental Data

	Volume ratio BTC			2-NSA concentration BTC		
Experiment index	Q(ml/min)	K(m^2)	ϕ	a_0	R_c ($kgm^{-3}s^{-1}$)	a_{wn}^{max} (m^{-1})
GB55_1_pp	0.73	6×10^{-13}	0.41	1.2×10^{-5}	3×10^{-12}	1,020
GB55_2_pp	0.67	6×10^{-13}	0.41	1.2×10^{-5}	3×10^{-12}	1,020
GB55_3_pp	0.7	6×10^{-13}	0.41	1.2×10^{-5}	3×10^{-12}	1,020
GB170_1_pp	0.55	8×10^{-12}	0.42	3×10^{-5}	3×10^{-12}	847
GB170_2_pp	0.74	8×10^{-12}	0.42	3×10^{-5}	3×10^{-12}	847
GB170_3_pp	0.65	8×10^{-12}	0.42	3×10^{-5}	1.2×10^{-11}	847
GB170_1_sp	1	8×10^{-12}	0.42	3×10^{-5}	1.2×10^{-11}	847
GB170_2_sp	1	8×10^{-12}	0.42	3×10^{-5}	1.2×10^{-11}	847
GB170_3_sp	1	8×10^{-12}	0.41	3×10^{-5}	1.2×10^{-11}	847
GB240_1_pp	0.49	1×10^{-12}	0.42	3×10^{-5}	1.2×10^{-11}	779
GB240_2_pp	0.76	1×10^{-12}	0.42	3×10^{-5}	1.2×10^{-11}	779
GB240_3_pp	0.75	1×10^{-12}	0.42	3×10^{-5}	1.2×10^{-11}	779
GB240_1_sp	1	1×10^{-12}	0.42	3×10^{-5}	1.2×10^{-11}	779
GB240_2_sp	1	1×10^{-12}	0.42	3×10^{-5}	1.2×10^{-11}	779
GB240_3_sp	1	1×10^{-12}	0.4	3×10^{-5}	1.2×10^{-11}	779
NS130_1_sp	1	5×10^{-13}	0.4	4×10^{-5}	1.2×10^{-11}	2,130
NS130_2_sp	1	5×10^{-13}	0.43	4×10^{-5}	1.2×10^{-11}	2,130
NS130_3_sp	1	5×10^{-13}	0.43	4×10^{-5}	1.2×10^{-11}	2,130
NS210_1_pp	0.73	7×10^{-14}	0.42	5×10^{-5}	3×10^{-12}	1,400
NS210_2_pp	0.76	7×10^{-14}	0.42	5×10^{-5}	3×10^{-12}	1,400
NS210_3_pp	0.76	7×10^{-14}	0.42	5×10^{-5}	3×10^{-12}	1,400
NS210_1_sp	1	7×10^{-14}	0.42	5×10^{-5}	1.2×10^{-11}	1,400
NS210_2_sp	1	7×10^{-14}	0.42	5×10^{-5}	1.2×10^{-11}	1,400
NS210_3_sp	1	7×10^{-14}	0.42	5×10^{-5}	1.2×10^{-11}	1,400
NS250_1_pp	0.8	5×10^{-12}	0.4	4×10^{-5}	1.2×10^{-11}	965
NS250_2_pp	0.85	5×10^{-12}	0.4	4×10^{-5}	1.2×10^{-11}	965
NS250_3_pp	0.5	5×10^{-12}	0.4	4×10^{-5}	1.2×10^{-11}	965

fitting to the experimental data, simulations with a sweep of the parameter a_0 in the polynomial Equation 7 are implemented to change the magnitude of the $a_{wn} - S_w$ curve while maintaining the shape of the curve (Tatomir et al., 2018). Generally, the overall trend of the experimental BTCs can be accounted for as linearly increasing, as it is predicted by the numerical models. The obtained a_0 values and the reaction rate of the tracer for all sands are shown in Table 3, and the corresponding $a_{wn} - S_w$ curves are shown in Figure 8.

While the overall trend of the experimental results matches the simulated curve in Figure 7, some temporal data points still display discrepancies. For several experiments, the last experimental data point (circled in gray in Figure 7) exhibits a lower concentration than this predicted by the model. This is mainly due to the fact that the water samples at late stages of the experiments (i.e., the ending of the displacement when the system is approaching the steady state) come from the remobilization of isolated trapped water inside the column. These isolated trapped zones are bypassed during the displacement, leading to a smaller FIFA compared to the FIFA averaged at the displacement front. As a result, remobilized water collected at a later stage of the experiment exhibits a smaller concentration. However, in the KIS tracer experiments, the main focus is on the water sample obtained from the front (i.e., samples shortly after breakthrough), as this is where the transition zone occurs, and where saturation changes over time. A previous pore-scale study by Gao et al. (2021a) confirmed that the FIFA at the front is only relevant to the tracer concentration in water belonging to the front and in direct proximity to the outflow. Generally, there are no more effective concentration data points when V_n/V of the effluent is larger than 0.9, indicating that the tracer test is finished. Therefore, concentration data obtained when V_n/V in the effluent is larger than 0.9 is not take into consideration. This also explains why there are fewer data points for the BTCs of 2-NSA concentration (in Figure 7) than the BTCs of the volume fraction of the non-wetting phase (in Figure 6) for the same experiments.

In Figure 7, the second y-axis (on the right side) was used for a tracer concentration of 0.5 g/l. In our previous study (Tatomir et al., 2018), we used the same glass beads of GB240 and ran four experiments with an initial KIS tracer concentration of 0.5 g/l. The results from Tatomir et al. (2018) provided a range of a_{wn}^{max} values: $4.1 < a_{wn}^{max} < 5.4$ cm^{-1}, $5.0 < a_{wn}^{max} < 7.5$ cm^{-1}, $3.0 < a_{wn}^{max} < 15$ cm^{-1} and $4.6 < a_{wn}^{max} < 11.5$ cm^{-1}. In comparison, the fitted results in Figure 8 give a_{wn}^{max} of 7.79 cm^{-1}, which falls within the range of our previous experiments. These results indicate a different tracer concentration does not affect the measurement if the reaction rate is accurately determined. Furthermore, the measured interfacial area (Figure 8) is much smaller than the calculated GSSA or SSSA-MIP (Table 1) for each type of sand or glass beads. This is a strong indication that the KIS tracer method measures the capillary-associated FIFA rather than the total FIFA including the films. Additionally, the slight difference in the shape of the a_{wn}–S_w curve is due to the difference in the P_c–S_w curve obtained from MIP measurements for each sand. To compare our results with literature data on measuring the capillary-associated interfacial area, we used the maximum value on the $p_c - S_w$ curve (a_{wn}^{max}) as an index for comparison (Tatomir et al., 2018).

3.3. Comparison of Measured Interfacial Area With Literature Data

To compare FIFA with literature data, it is necessary to consider the type of FIFA being compared, that is, total or capillary-associated FIFA, as well as the porous medium-fluids system types used in the experiments. Most commonly, the fluid-systems used in the reported experiments are air-water and, less often, NAPL-water. To the authors' knowledge there are only four studies that report the measured specific capillary-associated FIFA

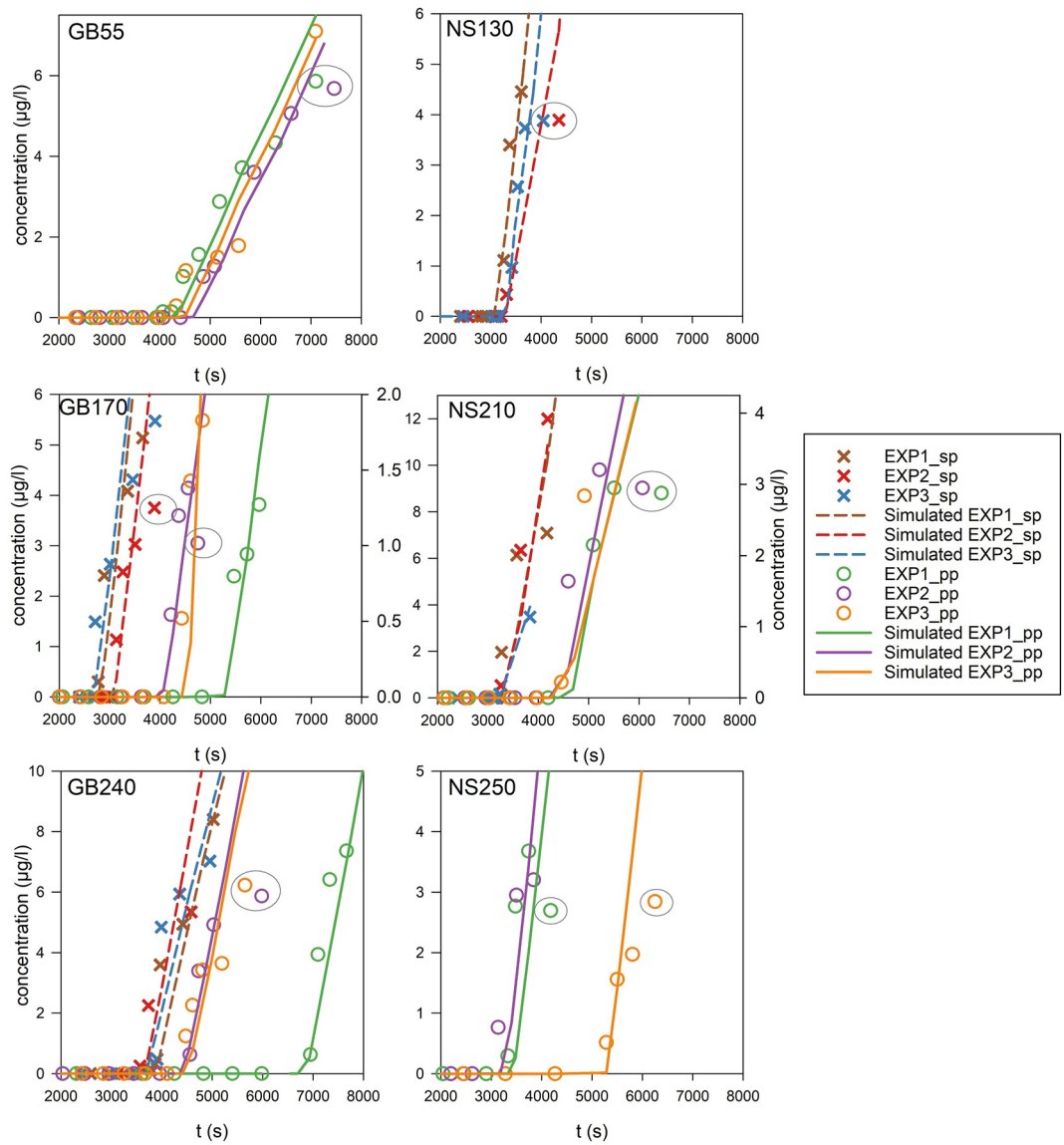

Figure 7. Plot of BTC of 2-NSA concentration (hydrolyzed KIS tracer) at column outlet versus time, for experimental data (crosses) and simulated BTCs (dashed lines) of triplicate experiments (EXP1, EXP2, and EXP3) with setup of the peristaltic pump (pp) and the syringe pump (sp). The experimental data points at late stage of the displacement showing some discrepancies from the modeling curves are circled in gray.

(Araujo & Brusseau, 2020; Brusseau et al., 2006; Culligan et al., 2006; Porter et al., 2010). XMT was used in each of these studies. In this study, we plot the maximum values of the capillary-associated specific interfacial area-saturation curves obtained from KIS tracer test and those reported in the literature versus the inverse median grain diameter (Figure 9).

Figure 9 compares the $a_{wn}^{\max}$ values obtained with the KIS tracer method and with XMT experiments using NAPL-water fluid system from (Culligan et al., 2006; Porter et al., 2010), and air-water fluid system from (Araujo & Brusseau, 2020; Brusseau et al., 2006). Likos and Jaafar (2013) developed a pore-geometry model that calculates the specific FIFA based on the measured grain-size distributions. They apply their model to four porous media (small glass beads, F75 Ottawa sand, large glass beads, river sand) and plot the capillary-associated FIFA, a_{wn}. Note that the capillary-associated FIFA determined by Culligan et al. (2006) for air-water (AW) was smaller than this from oil-water (OW) fluid systems in the same porous medium during primary drainage. The XMT revealed that air is located in larger continuous fluid configurations while the oil forms smaller, less

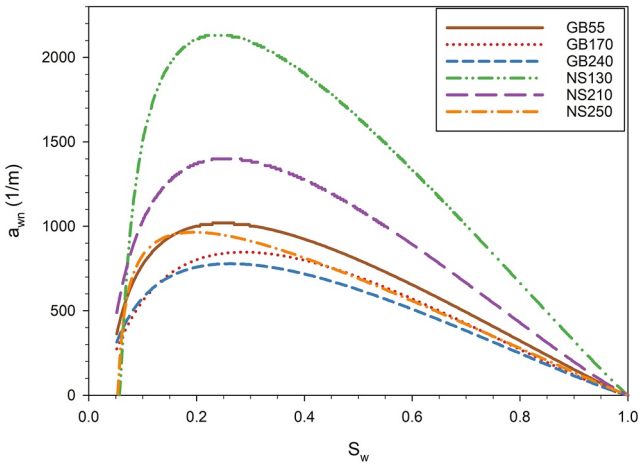

Figure 8. Plot of the specific capillary-associated FIFA versus saturation, $a_{wn} - S_w$ relations, for the six porous media.

well-connected configurations at similar saturations, leading to larger interfacial areas. Here, we do not apply any scaling to a_{wn} values.

The results in Figure 9 show that, at the same grain sizes, both the Grant and Gerhard and the Likos and Jaafar models predict a larger capillary-associated FIFA than that measured from the KIS tracer test. Both models predict an increasing trend of capillary-associated FIFA when the IMGD is larger. However, the KIS measured capillary-associated FIFA for glass beads with different sizes are close to each other, and it matches the results from (Araujo & Brusseau, 2020), even though the size of glass beads they use is larger. Implementing a linear regression over the $a_{nw}^{\max} -$ IMGD data, we obtain the following relation for the glass-beads material:

$$a_{wn}^{\max} = \frac{0.016}{d_{50}} + 7.31 \tag{15}$$

The observed slope of the curve indicates that the grain size has a negligible effect on the capillary-associated FIFA for glass-beads. This could be attributed to the high roundness factor of all three glass beads, and the formation of unconsolidated porous media with similar porosities (ranging from 40% to 43%), as shown in Table 3. Brusseau et al. (2010) reported a strong correlation between the total specific FIFA, a_n, its related, a_{wn}, and the IMGD. This observation is not in conflict with the results from this study, since the majority of total specific interfacial area is associated with films, and is highly dependent on the solid surface area and the grain size. On the smooth surfaces of glass beads, the adsorbed water film (with a thickness of only a few molecules) depletes fast due to the hydrolysis reaction with the tracer (Gao et al., 2023), and therefore these water films contribute very little to the overall results. In this case, the KIS tracer method excludes the film-associated interfacial area and only measures the capillary-associated FIFA. An assembly of the total interfacial area (in $a_n^{\max}$) and the capillary-associated interfacial area (in $a_{wn}^{\max}$) measured from literature are given in Figure S3 of Supporting Information S1.

Furthermore, Figure 9 shows that only the coarsest natural sand has a similar capillary-associated FIFA with the glass beads, while for the other two finer natural sands the capillary-associated FIFA measured with KIS

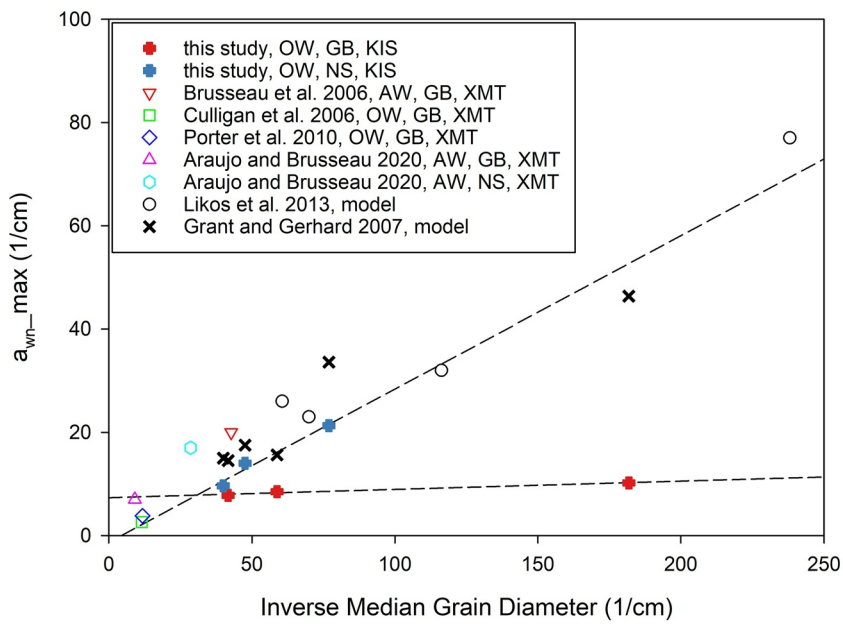

Figure 9. Plot of $a_{wn}^{\max}$ (maximum capillary-associated interfacial area) determined by KIS tracer experiment in an *n*-octane-water fluid system and comparison with literature data for capillary-associated interfacial area. Dashed lines are the regression lines for KIS tracer measurement for glass beads and natural soils.

tracer is larger than the results of glass beads. This is attributed to the rough surfaces of the natural sands. The pore-scale study by Gao et al. (2021b) showed that the bursting process during Haines jumps induced by rough grain surfaces can significantly increase the capillary-associated (mobile) FIFA at the front. Besides, this finding is also in agreement with Brusseau et al. (2009) and consistent with the results of Araujo and Brusseau (2020) for measurements at the steady-state. Implementing a linear regression over the $a_{nw}^{\max} - \text{IMGD}$ data we obtain the following relation for the natural sands:

$$a_{wn}^{\max} = \frac{0.297}{d_{50}} - 1.307 \tag{16}$$

In contrast to the results for glass beads, the $a_{wn}^{\max}$ for natural sands follow a linearly increasing trend with an increase in IMGD, indicating that the measured capillary-associated FIFA for natural sands can be associated with the solid surface area. The slope of the linear regression line follows the overall increasing trend predicted by the models of Grant and Gerhard (2007) and Likos and Jaafar (2013). This trend may be attributed to the introduction of corner interfaces and capillary condensed water on rough surface of the natural sand samples, which have low roundness and irregular shapes (as shown in Figure 3). This causes the increase of the production of tracer reaction product due to the increase of the capillary-associated interfaces at the front.

4. Conclusions

In this study, we demonstrated the potential of the KIS tracer technique as a robust and effective technique for characterizing capillary-associated fluid–fluid interfaces during (dynamic) two-phase displacement processes in porous-media-filled columns. By performing 27 sets of measurements on six different porous media (glass beads and natural soils of different grain sizes), we were able to test and successfully extend the range of applicability of the KIS tracers beyond the one type of glass-beads material previously studied.

Our main findings are summarized below.

- The two-phase flow model is capable of predicting the fluid volumes ratio BTCs, with good accuracy. However, small deviations are observed in the experiments conducted with natural soil NS210. The model tends to slightly underestimate the non-wetting phase to total fluid volume ratio in the experiments with high capillary number.
- By assuming the shapes of the $a_{wn} - S_w$ curves according to the model proposed by Grant and Gerhard (2007), the reactive transport model is capable of replicating the experimentally obtained concentration data. Furthermore, the model accurately captures the overall increasing trend of the tracer concentration breakthrough curves.
- With the $a_{wn} - S_w$ curves assuming the shapes following the model from Grant and Gerhard (2007), the results from the reactive transport model can match the experimentally measured concentration, and the overall increasing trend of the data is captured. The deviations of some data points between modeling and experimental results are mainly found at late stages of the breakthrough due to the remobilization of the trapped water.
- By comparing the measured and interpreted data presented in this study with literature data, valuable insights into the characterization of the fluid–fluid/NAPL-water interfaces were further gained. In particular, the findings suggest that for porous media composed of glass beads with similar porosity, a decrease in the grain size does not result in a significant increase in the measured specific capillary-associated FIFA.
- The maximum specific capillary-associated FIFA, as measured by the KIS tracer, increases linearly with the inverse mean grain diameter for the porous media composed of natural soils. This linear relation follows a trend similar to the model reported by Grant and Gerhard (2007) and Likos and Jaafar (2013). Furthermore, it was observed that natural sands exhibit larger capillary-associated FIFA compared to glass beads, which is consistent with the observations made for the total specific FIFA. For natural soils characterized by rough surfaces and irregular shapes, the capillary-associated FIFA increases linearly with an increase in the inverse mean grain diameter.

Our study represents a crucial step toward establishing KIS tracer as a robust characterization technique capable of measuring capillary-associated fluid–fluid interfacial area in multiphase flow in porous media systems. The KIS tracer has a potential to be used in practical applications where a transient non-wetting phase fluid flooding is involved. For example, in geological storage of carbon dioxide, the KIS tracer can be used during (supercritical)

CO_2 injection to monitor the movement of plume and the saturations distributions of the CO_2 through measuring the FIFA. The KIS tracer can also be applied in laboratory experiments to estimate the FIFA during infiltration of NAPL contaminants into the aquifer, for example, KIS tracer experiment setup with approximate flow conditions and the medium excavated from the site.

Further research is required to extend the application of KIS tracer and investigate their reactive transport in two-dimensional or three-dimensional systems, considering the effects of porous media heterogeneity and fluid density. Additionally, extending the applicability of the method to a wider range of flow conditions and fluid–fluid-porous media systems (e.g., super critical CO_2 water) is required before applying the technique in real-field conditions. Besides, it is worth to further research about study the system in a dimensionless format. This approach can unveil systematic behavior and provide valuable insight into the underlying patterns.

Nomenclature

Symbol	Parameter name	Unit
a_{wn}	Specific fluid-fluid interfacial area	1/m
$a_{wn}^{\max}$	Maximum specific fluid-fluid interfacial area	1/m
a_0, a_1, a_2, a_3	Fitting parameter for the polynomial Equation 7	–
a_L	Longitudinal dispersivity	m
a_T	Transversal dispersivity	m
c_w^κ	2-NSA concentration in water	µg/L
C_u	Grain size uniformity	–
d_m	Grain mean diameter	µm
d_{50}	Mean grain size	cm
$D_{pm,w}^\kappa$	Dispersion coefficient	m^2/s
K	Intrinsic permeability	m^2
k_{rw}	Relative permeability of wetting phase	–
k_{rn}	Relative permeability of non-wetting phase	–
p	pressure	Pa
P_u	Pore size uniformity	–
P_d	Entry pressure	Pa
P_c	Capillary pressure	Pa
$p_c^{\max}$	Maximum capillary pressure	Pa
Q	Flow rate	mL/min
$R_{cn\to w}^\kappa$	Reaction rate constant	$kg\ s^{-1}m^{-2}$
$r_{n\to w}^\kappa$	Reaction rate	$kg\ s^{-1}m^{-3}$
S_w	Wetting phase saturation	–
S_{wr}	Residual wetting phase saturation	–
S_n	Non-wetting phase saturation	–
S_e	Effective saturation	–
v	Darcy velocity	m/s
V	Total effluent volume	mL/min
V_n	Non-wetting phase effluent volume	mL/min
ϕ	Porosity	–
θ	Contact angle	–
σ	Interfacial tension	N/m
λ	Pore index coefficient (Brooks-Corey)	–

Symbol	Parameter name	Unit
ρ	Fluid density	kg/m^3
ρ_p	Particle density	kg/m^3
μ	Dynamic viscosity	Pa•s
Acronyms		
AW	Air-water	
BTC	Breakthrough curve	
FIFA	Fluid-fluid interfacial area	
GB	Glass beads	
GSSA	Geometric smooth-sphere specific solid surface area	
IPTT	Interface partitioning tracer test	
IMGD	Inverse median grain diameter	
KIS	Kinetic Interface Sensitive	
MIP	Mercury-intrusion porosimetry	
N_2/BET	Nitrogen Brunauer–Emmett–Teller method	
NS	Natural sands	
NAPL	Non-aqueous phase liquid	
OW	Oil-water	
pp	Peristaltic pump	
sp	Syringe pump	
SSSA	Specific solid surface area	
XMT	X-ray microtomography	

Data Availability Statement

The data on which this article is based are available in Tatomir et al. (2023).

Acknowledgments
This project was funded by the German Research Foundation, DFG, under project number 428614366. We are grateful to Florian Duschl and Dejian Zhou for the support with the laboratory work. HS and NK would like to thank the Deutsche Forschungsgemeinschaft (DFG, German Research Foundation) for supporting this work by funding SFB 1313, Project Number 327154368. HS and NK would like to thank the Deutsche Forschungsgemeinschaft (DFG, German Research Foundation) under Germany's Excellence Strategy—EXC 2075–390740016. They also acknowledge the support by the Stuttgart Center for Simulation Science (SimTech).

References

Annable, M. D., Rao, P. S. C., Hatfield, K., Graham, W. D., Wood, A. L., & Enfield, C. G. (1998). Partitioning tracers for measuring residual NAPL: Field-scale test results. *Journal of Environmental Engineering*, *124*(6), 498–503. https://doi.org/10.1061/(ASCE)0733-9372

Anwar, A. H. M. F., Bettahar, M., & Matsubayashi, U. (2000). A method for determining air–water interfacial area in variably saturated porous media. *Journal of Contaminant Hydrology*, *43*, 129–146. https://doi.org/10.1016/S0169-7722(99)00103-5

Araujo, J. B., & Brusseau, M. L. (2020). Assessing XMT-measurement variability of air-water interfacial areas in natural porous media. *Water Resources Research*, *56*, e2019WR025470. https://doi.org/10.1029/2019WR025470

Armstrong, R. T., McClure, J. E., Berrill, M. A., Rücker, M., Schlüter, S., & Berg, S. (2016). Beyond Darcy's law: The role of phase topology and ganglion dynamics for two-fluid flow. *Physical Review E - Statistical Physics, Plasmas, Fluids, and Related Interdisciplinary Topics*, *94*, 043113. https://doi.org/10.1103/PhysRevE.94.043113

Aursjo, O., Erpelding, M., Tallakstad, K. T., Flekkøy, E. G., Hansen, A., & Maloy, K. J. (2014). Film flow dominated simultaneous flow of two viscous incompressible fluids through a porous medium. *Frontiers in Physics*, *2*(63), 1–9. https://doi.org/10.3389/fphy.2014.00063

Bradford, S. A., & Leij, F. J. (1997). Estimating interfacial areas for multi-fluid soil systems. *Journal of Contaminant Hydrology*, *27*, 83–105. https://doi.org/10.1016/S0169-7722(96)00048-4

Brooks, R. H., & Corey, A. T. (1964). *Hydraulic properties of porous media*. *Hydrology Paper* (Vol. 33). Colorado State University.

Brusseau, M. L. (2018). Assessing the potential contributions of additional retention processes to PFAS retardation in the subsurface. *Science of the Total Environment*, *613–614*, 176–185. https://doi.org/10.1016/j.scitotenv.2017.09.065

Brusseau, M. L. (2019). The influence of molecular structure on the adsorption of PFAS to fluid-fluid interfaces: Using QSPR to predict interfacial adsorption coefficients. *Water Research*, *152*, 148–158. https://doi.org/10.1016/j.watres.2018.12.057

Brusseau, M. L., Janousek, H., Murao, A., & Schnaar, G. (2008). Synchrotron X-ray microtomography and interfacial partitioning tracer test measurements of NAPL-water interfacial areas. *Water Resources Research*, *44*, W01411. https://doi.org/10.1029/2006WR005517

Brusseau, M. L., Narter, M., & Janousek, H. (2010). Interfacial partitioning tracer test measurements of organic-liquid/water interfacial areas: Application to soils and the influence of surface roughness. *Environmental Science Technology*, *44*, 7596–7600. https://doi.org/10.1021/es101312n

Brusseau, M. L., Narter, M., Schnaar, G., & Marble, J. (2009). Measurement and estimation of organic-liquid/water interfacial areas for several natural porous media. *Environmental Science Technology*, *43*, 3619–3625. https://doi.org/10.1021/es8020827

Brusseau, M. L., Ouni, A. E., Araujo, J. B., & Zhong, H. (2015). Novel methods for measuring air–water interfacial area in unsaturated porous media. *Chemosphere*, *127*, 208–213. https://doi.org/10.1016/j.chemosphere.2015.01.029

Brusseau, M. L., Peng, S., Schnaar, G., & Costanza-Robinson, M. S. (2006). Relationships among air-water interfacial area, capillary pressure, and water saturation for a sandy porous medium. *Water Resources Research*, *42*, W03501. https://doi.org/10.1029/2005WR004058

Brusseau, M. L., Peng, S., Schnaar, G., & Murao, A. (2007). Measuring air−water interfacial areas with X-ray microtomography and interfacial partitioning tracer tests. *Environmental Science Technology*, *41*, 1956–1961. https://doi.org/10.1021/es061474m

Burdine, N. T. (1953). Relative permeability calculations from pore size distribution data. *Journal of Petroleum Technology*, *5*(03), 71–78.

Cary, J. W. (1994). Estimating the surface area of fluid phase interfaces in porous media. *Journal of Contaminant Hydrology*, *15*, 243–248. https://doi.org/10.1016/0169-7722(94)90029-9

Cho, J., & Annable, M. D. (2005). Characterization of pore scale NAPL morphology in homogeneous sands as a function of grain size and NAPL dissolution. *Chemosphere*, *61*, 899–908. https://doi.org/10.1016/j.chemosphere.2005.04.042

Costanza, M. S., & Brusseau, M. L. (2000). Contaminant vapor adsorption at the gas−water interface in soils. *Environmental Science Technology*, *34*, 1–11. https://doi.org/10.1021/es9904585

Costanza-Robinson, M. S., & Brusseau, M. L. (2002). Air-water interfacial areas in unsaturated soils: Evaluation of interfacial domains. *Water Resources Research*, *38*, 1195. https://doi.org/10.1029/2001WR000738

Culligan, K. A., Wildenschild, D., Christensen, B. S. B., Gray, W. G., & Rivers, M. L. (2006). Pore-scale characteristics of multiphase flow in porous media: A comparison of air–water and oil–water experiments. *Advances in Water Resources*, *29*, 227–238. https://doi.org/10.1016/j.advwatres.2005.03.021

Dalla, E., Hilpert, M., & Miller, C. T. (2002). Computation of the interfacial area for two-fluid porous medium systems. *Journal of Contaminant Hydrology*, *56*, 25–48.

Dobson, R., Schroth, M. H., Oostrom, M., & Zeyer, J. (2006). Determination of NAPL−Water interfacial areas in well-characterized porous media. *Environmental Science Technology*, *40*, 815–822. https://doi.org/10.1021/es050037p

Flemisch, B., Darcis, M., Erbertseder, K., Faigle, B., Lauser, A., Mosthaf, K., et al. (2011). DuMux: DUNE for multi-{phase, component, scale, physics, …} flow and transport in porous media. *Advances in Water Resources*, *34*, 1102–1112. https://doi.org/10.1016/j.advwatres.2011.03.007

Fukunishi, Y., Tateishi, T., & Suzuki, M. (1996). Octane/water interfacial tension calculation by molecular dynamics simulation. *Journal of Colloid and Interface Science*, *180*, 188–192. https://doi.org/10.1006/jcis.1996.0288

Gao, H., Tatomir, A. B., Karadimitriou, N. K., Steeb, H., & Sauter, M. (2021a). A two-phase, pore-scale reactive transport model for the kinetic interface-sensitive tracer. *Water Resources Research*, *57*, e2020WR028572. https://doi.org/10.1029/2020WR028572

Gao, H., Tatomir, A. B., Karadimitriou, N. K., Steeb, H., & Sauter, M. (2021b). Effects of surface roughness on the kinetic interface-sensitive tracer transport during drainage processes. *Advances in Water Resources*, 104044. https://doi.org/10.1016/j.advwatres.2021.104044

Gao, H., Tatomir, A. B., Karadimitriou, N. K., Steeb, H., & Sauter, M. (2023). Reservoir characterization by push-pull tests employing kinetic interface sensitive tracers - A pore-scale study for understanding large-scale processes. *Advances in Water Resources*, *174*, 104424. https://doi.org/10.1016/j.advwatres.2023.104424

Grant, G. P., & Gerhard, J. I. (2007). Simulating the dissolution of a complex dense nonaqueous phase liquid source zone: 1. Model to predict interfacial area. *Water Resources Research*, *43*, W12410. https://doi.org/10.1029/2007WR006038

Gvirtzman, H., & Roberts, P. V. (1991). Pore scale spatial analysis of two immiscible fluids in porous media. *Water Resources Research*, *27*, 1165–1176. https://doi.org/10.1029/91WR00303

Hassanizadeh, S. M., & Gray, W. G. (1990). Mechanics and thermodynamics of multiphase flow in porous media including interphase boundaries. *Advances in Water Resources*, *13*, 169–186. https://doi.org/10.1016/0309-1708(90)90040-B

Hassanizadeh, S. M., & Gray, W. G. (1993). Thermodynamic basis of capillary pressure in porous media. *Water Resources Research*, *29*, 3389–3405. https://doi.org/10.1029/93WR01495

Held, R. J., & Celia, M. A. (2001). Pore-scale modeling extension of constitutive relationships in the range of residual saturations. *Water Resources Research*, *37*, 165–170. https://doi.org/10.1029/2000WR900234

Helmig, R. (1997). *Multiphase flow and transport processes in the subsurface: A contribution to the modeling of hydrosystems*. Springer.

Jiang, H., Guo, B., & Brusseau, M. L. (2020). Pore-scale modeling of fluid-fluid interfacial area in variably saturated porous media containing microscale surface roughness. *Water Resources Research*, *56*, e2019WR025876. https://doi.org/10.1029/2019WR025876

Joekar-Niasar, V., & Hassanizadeh, S. M. (2012). Uniqueness of specific interfacial area–capillary pressure–saturation relationship under non-equilibrium conditions in two-phase porous media flow. *Transport in Porous Media*, *94*, 465–486. https://doi.org/10.1007/s11242-012-9958-3

Karadimitriou, N. K., Joekar-Niasar, V., Babaei, M., & Shore, C. A. (2016). Critical role of the immobile zone in non-Fickian two-phase transport: A new paradigm. *Environmental Science Technology*, *50*, 4384–4392. https://doi.org/10.1021/acs.est.5b05947

Kim, H., Rao, P. S. C., & Annable, M. D. (1997). Determination of effective air-water interfacial area in partially saturated porous media using surfactant adsorption. *Water Resources Research*, *33*, 2705. https://doi.org/10.1029/97WR02227

Kim, H., Rao, P. S. C., & Annable, M. D. (1999). Gaseous tracer technique for estimating air–water interfacial areas and interface mobility. *Soil Science Society of America Journal*, *63*, 1554–1560. https://doi.org/10.2136/sssaj1999.6361554x

Lenormand, R., Touboul, E., & Zarcone, C. (1988). Numerical models and experiments on immiscible displacements in porous media. *Journal of Fluid Mechanics*, *189*, 165–187. https://doi.org/10.1017/S0022112088000953

Leverett, M. C. (1941). Capillary behavior in porous solids. *Transanctions of AIME*, *142*, 152–169. https://doi.org/10.2118/941152-G

Likos, W. J., & Jaafar, R. (2013). Pore-scale model for water retention and fluid partitioning of partially saturated granular soil. *Journal of Geotechnical Geoenvironmental Enginnering*, *139*, 724–737. https://doi.org/10.1061/(ASCE)GT.1943-5606.0000811

McDonald, K., Carroll, K. C., & Brusseau, M. L. (2016). Comparison of fluid-fluid interfacial areas measured with X-ray microtomography and interfacial partitioning tracer tests for the same samples. *Water Resources Research*, *52*, 5393–5399. https://doi.org/10.1002/2016WR018775

Meakin, P., & Tartakovsky, A. M. (2009). Modeling and simulation of pore-scale multiphase fluid flow and reactive transport in fractured and porous media. *Reviews of Geophysics*, *47*. https://doi.org/10.1029/2008RG000263

Miller, C. T., Poirier-McNeil, M. M., & Mayer, A. S. (1990). Dissolution of trapped nonaqueous phase liquids: Mass transfer characteristics. *Water Resources Research*, *26*, 2783–2796. https://doi.org/10.1029/WR026i011p02783

Narter, M., & Brusseau, M. L. (2010). Comparison of Interfacial partitioning tracer test and high-resolution microtomography measurements of fluid-fluid interfacial areas for an ideal porous medium. *Water Resources Research*, *46*. https://doi.org/10.1029/2009WR008375

Nelson, N. T., & Brusseau, M. L. (1996). Field study of the partitioning tracer method for detection of dense nonaqueous phase liquid in a trichloroethene- contaminated aquifer. *Environmental Science Technology*, *30*, 2859–2863. https://doi.org/10.1021/es960148b

Niemi, A., Bensabat, J., Shtivelman, V., Edlmann, K., Gouze, P., Luquot, L., et al. (2016). Heletz experimental site overview, characterization and data analysis for CO_2 injection and geological storage. *International Journal of Greenhouse Gas Control*, *48*, 3–23. https://doi.org/10.1016/j.ijggc.2015.12.030

Oostrom, M., White, M. D., & Brusseau, M. L. (2001). Theoretical estimation of free and entrapped nonwetting–wetting fluid interfacial areas in porous media. *Advances in Water Resources*, *24*, 87–898. https://doi.org/10.1016/S0309-1708(01)00017-3

Patmonoaji, A., Tsuji, K., Muharrik, M., & Suekane, T. (2018). Micro-tomographic analyses of specific interfacial area inside unconsolidated porous media with differing particle characteristics from microscopic to macroscopic scale. *Journal of Colloid and Interface Science*, *532*, 614–621. https://doi.org/10.1016/j.jcis.2018.08.023

Peche, A., Halisch, M., Bogdan Tatomir, A., & Sauter, M. (2016). Development of a numerical workflow based on µ-CT imaging for the determination of capillary pressure–saturation-specific interfacial area relationship in 2-phase flow pore-scale porous-media systems: A case study on Heletz sandstone. *Solid Earth*, *7*, 727–739. https://doi.org/10.5194/se-7-727-2016

Peng, S., & Brusseau, M. L. (2005). Impact of soil texture on air-water interfacial areas in unsaturated sandy porous media. *Water Resources Research*, *41*. https://doi.org/10.1029/2004WR003233

Porter, M. L., Wildenschild, D., Grant, G., & Gerhard, J. I. (2010). Measurement and prediction of the relationship between capillary pressure, saturation, and interfacial area in a NAPL-water-glass bead system. *Water Resources Research*, *46*, W08512. https://doi.org/10.1029/2009WR007786

Reeves, P. C., & Celia, M. A. (1996). A functional relationship between capillary pressure, saturation, and interfacial area as revealed by a pore-scale network model. *Water Resources Research*, *32*, 2345. https://doi.org/10.1029/96WR01105

Rootare, H. M., & Prenzlow, C. F. (1967). Surface areas from mercury porosimeter measurements. *The Journal of Physical Chemistry A*, *71*, 2733–2736. https://doi.org/10.1021/j100867a057

Saripalli, K. P., Kim, H., Rao, P. S. C., & Annable, M. D. (1997). Measurement of specific Fluid−Fluid interfacial areas of immiscible fluids in porous media. *Environmental Science Technology*, *31*, 932–936. https://doi.org/10.1021/es960652g

Schaffer, M., Maier, F., Licha, T., & Sauter, M. (2013). A new generation of tracers for the characterization of interfacial areas during supercritical carbon dioxide injections into deep saline aquifers: Kinetic interface-sensitive tracers (KIS tracer). *International Journal of Greenhouse Gas Control*, *14*, 200–208. https://doi.org/10.1016/j.ijggc.2013.01.020

Schnaar, G., & Brusseau, M. L. (2006). Characterizing pore-scale configuration of organic immiscible liquid in multiphase systems with synchrotron X-ray microtomography. *Vadose Zone Journal*, *5*, 641–648. https://doi.org/10.2136/vzj2005.0063

Simon, M. A., & Brusseau, M. L. (2007). Analysis of a gas-phase partitioning tracer test conducted in an unsaturated fractured-clay formation. *Journal of Contaminant Hydrology*, *90*, 146–158. https://doi.org/10.1016/j.jconhyd.2006.09.010

Tatomir, A., Gao, H., & Abdullah, H. (2023). Data for "Estimation of capillary-associated NAPL-Water interfacial areas for unconsolidated porous media by kinetic interface sensitive (KIS) tracer method" [Dataset]. Figshare. https://doi.org/10.6084/m9.figshare.24492382

Tatomir, A., Maier, F., Schaffer, M., Licha, T., & Sauter, M. (2013). Modelling of kinetic interface sensitive tracers for two-phase systems. In M. Z. Hou, H. Xie, & P. Were (Eds.), *Clean energy systems in the subsurface: Production, storage and conversion* (pp. 65–74). Springer Berlin Heidelberg.

Tatomir, A., Vriendt, K. D., Zhou, D., Gao, H., Duschl, F., Sun, F., et al. (2018). Kinetic interface sensitive tracers: Experimental validation in a two-phase flow column experiment. A proof of concept. *Water Resources Research*, *54*, 10223–10241. https://doi.org/10.1029/2018WR022621

Tatomir, A. B., Halisch, M., Duschl, F., Peche, A., Wiegand, B., Schaffer, M., et al. (2016). An integrated core-based analysis for the characterization of flow, transport and mineralogical parameters of the Heletz pilot CO_2 storage site reservoir. *International Journal of Greenhouse Gas Control*, *48*(1), 24–43. https://doi.org/10.1016/j.ijggc.2016.01.030

Tatomir, A. B., Jyoti, A., & Sauter, M. (2016). The monitoring of CO_2 plume migration in deep saline formations with kinetic interface sensitive tracers. In T. N. Singh & V. Vikram (Eds.), *Geologic carbon Sequestration: Understanding reservoir concepts* (p. 336). Springer.

Tatomir, A. B., Schaffer, M., Kissinger, A., Hommel, J., Nuske, P., Licha, T., et al. (2015). Novel approach for modeling kinetic interface-sensitive (KIS) tracers with respect to time-dependent interfacial area change for the optimization of supercritical carbon dioxide injection into deep saline aquifers. *International Journal of Greenhouse Gas Control*, *33*, 145–153. https://doi.org/10.1016/j.ijggc.2014.11.020

Valavanides, M. S., Mascle, M., Youssef, S., & Vizika, O. (2020). Steady state two-phase flow in porous media: Laboratory validation of flow dependent relative permeability scaling. *The International Symposium of the Society of Core Analysts (SCA2019), E3S Web of Conferences*, *146*, 03002. https://doi.org/10.1051/e3sconf/202014603002

Ying, L., Brusseau Mark, L., El Asma, O., Araujo Juliana, B., & Su, X. (2017). The gas-absorption/chemical-reaction method for measuring air-water interfacial area in natural porous media. *Water Resources Research*, *53*, 9519–9527. https://doi.org/10.1002/2017WR021717

Zhong, H., El Ouni, A., Lin, D., Wang, B., & Brusseau, M. L. (2016). The two-phase flow IPTT method for measurement of nonwetting-wetting liquid interfacial areas at higher nonwetting saturations in natural porous media. *Water Resources Research*, *52*, 5506–5515. https://doi.org/10.1002/2016WR018783

References From the Supporting Information

Schaefer, C. E., DiCarlo, D. A., & Blunt, M. J. (2000). Determination of water-oil interfacial area during 3-phase gravity drainage in porous media. *Journal of Colloid and Interface Science*, *221*, 308–312. https://doi.org/10.1006/jcis.1999.6604

Washburn, E. W. (1921). Note on a method of determining the distribution of pore sizes in a porous material. *Proceedings of the National Academy of Sciences of the United States of America*, *7*(4), 115–116.